Title

Internal structure of the San Jacinto fault zone at the Ramona Reservation, north of Anza, California, from dense array seismic data

Journal
Geophysical Journal International, 224(2)

ISSN
0956-540X

Authors
Qin, Lei
Share, Pieter-Ewald
Qiu, Hongrui
et al.

Publication Date
2020-11-27

DOI
10.1093/gji/ggaa482

Peer reviewed

Internal structure of the San Jacinto fault zone at the Ramona Reservation, north of Anza, California, from dense array seismic data

Journal:	*Geophysical Journal International*
Manuscript ID	GJI-S-20-0385.R1
Manuscript Type:	Research Paper
Date Submitted by the Author:	n/a

Complete List of Authors:	Qin, Lei; University of Southern California, Department of Earth Sciences Share, Pieter-Ewald; University of California San Diego Scripps Institution of Oceanography, IGPP Qiu, Hongrui; Rice University, Department of Earth, Environmental and Planetary Sciences Allam, Amir A.; The University of Utah, Department of Geology and Geophysics Vernon, Frank; University of California San Diego Scripps Institution of Oceanography, IGPP Ben-Zion, Yehuda; University of Southern California, Department of Earth Sciences

Keywords:	Crustal imaging < SEISMOLOGY, Interface waves < SEISMOLOGY, Guided waves < SEISMOLOGY, Body waves < SEISMOLOGY, Seismic attenuation < SEISMOLOGY, Earthquake dynamics < SEISMOLOGY

Internal structure of the San Jacinto fault zone at the Ramona Reservation, north of Anza, California, from dense array seismic data

L. Qin[1], P.-E. Share[2], H. Qiu[3], A. A. Allam[4], F. L. Vernon[2] and Y. Ben-Zion[1,5]

[1]Department of Earth Sciences, University of Southern California, Los Angeles, CA, 90089, USA

[2]Scripps Institution of Oceanography, University of California San Diego, La Jolla, CA, 92093, USA

[3]Department of Earth, Environmental and Planetary Sciences, Rice University, Houston, TX, 77005, USA

[4]Department of Geology and Geophysics, University of Utah, Salt Lake City, UT, 84112, USA

[5]Southern California Earthquake Center, University of Southern California, Los Angeles, CA, 90089, USA

Geophysics Journal International

In review, 2020

Short title: Internal structure of the SJFZ

Summary

We image the internal structure of the San Jacinto fault zone (SJFZ) near Anza, California, with seismic data recorded by two dense arrays (RA and RR) from ~42,000 local and ~180 teleseismic events occurring between 2012-2017. The RA linear array has short aperture (~470 m long with 12 strong motion sensors) and recorded for the entire analyzed time window, whereas the RR is a large three-component nodal array (97 geophones across a ~2.4 km x 1.4 km area) that operated for about a month in September-October 2016. The SJFZ at the site contains three near-parallel surface traces F1, F2, and F3 from SW to NE that have accommodated several M_w>6 earthquakes in the past 15,000 years. Waveform changes in the fault normal direction indicate structural discontinuities that are consistent with the three fault surface traces. Relative slowness from local events and delay time analysis of teleseismic arrivals in the fault normal direction suggest a slower SW side than the NE with a core damage zone between F1 and F2. This core damage zone causes ~0.05 second delay at stations RR26-31 in the teleseismic P arrivals compared with the SW-most station, and generates both P- and S- type fault zone trapped waves. Inversion of S trapped waves indicates the core damaged structure is ~100 m wide, ~4 km deep with a Q value of ~20 and 40% S-wave velocity reduction compared with bounding rocks. Fault zone head waves observed at stations SW of F3 indicate a local bimaterial interface that separates the locally faster NE block from the broad damage zone in the SW at shallow depth and merges with a deep interface that separates the regionally faster NE block from rocks to the SW with slower velocities at greater depth. The multi-scale structural components observed at the site are related to the geological and earthquake rupture history at the site, and provide important information on the preferred NW propagation of earthquake ruptures on the San Jacinto fault.

Keywords: Crustal Imaging, Interface waves, Guided waves, Body waves, Seismic Attenuation, Earthquake dynamics

1 Introduction

Large fault zones often have large-scale bimaterial interfaces that separate two crustal blocks with different seismic velocities and hierarchical damage zones having reduction of elastic properties with respect to the bounding rocks (Ben-Zion & Sammis 2003, and references therin).

A large-scale bimaterial fault interface may induce preferential rupture propagation direction related to the velocity contrast and sense of loading (e.g., Weertman 1980, Andrews & Ben-Zion 1997, Ben-Zion 2001, Shlomai & Fineberg 2016). Numerous such ruptures on a given fault section are expected to generate asymmetric rock damage with the regionally faster block sustaining most of the damage (Ben-Zion & Shi 2005, Xu *et al.* 2012). The asymmetric fault damage zone may include pulverized rocks that provide important information on the generating dynamic strain field (Dor *et al.* 2006, Mitchell *et al.* 2011, Xu & Ben-Zion 2017) and is typically concentrated in the top few kilometers of the crust (e.g. Peng *et al.* 2003, Lewis *et al.* 2005). Information on bimaterial fault interfaces, damage zones and other fault properties can be obtained through high-density deployments of seismic instruments within and around the fault zone (Harjes & Henger 1973, Rost & Thomas 2002, Ben-Zion *et al*. 2015).

Located in the highly populated Southern California area, the San Jacinto fault zone (SJFZ) is one of the most seismically active fault zones along the boundary between the American and Pacific plates in the region (e.g. Hauksson *et al.* 2012, Ross *et al.* 2017) and accommodates a comparable potion of the plate motion to that of the southern San Andreas fault (e.g., Becker *et al.* 2005, Fay & Humphreys 2005, Lindsey & Fialko 2013). Historical records indicate that the SJFZ hosted numerous $M_w > 7$ earthquakes (Petersen & Wesnousky 1994, Rockwell *et al.* 2015), some rupturing most of the length of the SJFZ in a single event (Salisbury *et al.* 2012, Onderdonk *et al.* 2013), thus posing significant seismic hazard to the area. Tomography imaging results of the SJFZ (Allam & Ben-Zion 2012, Allam *et al.* 2014a, Share *et al.* 2019a) with nominal resolution of 1-2 km indicate complex structures with broad damage zones and various large-scale velocity contrasts across the fault.

To obtain high-resolution information on internal fault structures, five linear dense arrays with 10-30 m station spacing were deployed across main traces of the SJFZ in the Blackburn Saddle (BB), Ramona Reservation (RA), Sage Brush Flat (SGB), Dry Wash (DW) and Jackass Flat (JF) sites (white and red triangles from NW to SE in Fig. 1a). Analyses of direct arrivals, fault zone head waves that propagate along bimaterial interfaces, and fault zone trapped waves generated by interference of internal reflections within core fault damage zones reveal high-resolution local velocity variations, extent and velocity contrasts of bimaterial interfaces, and seismic and geometrical properties of damage zones at these sites (Qiu *et al.* 2017, Share *et al.* 2017, Qin *et al.* 2018, Share *et al.* 2019b). In addition, Zigone *et al.* (2019) used 2-35 Hz high-frequency noise data from these linear dense arrays to obtain shear wave velocities (0.3-0.9 km/s) in the top ~100 m.

To complement these studies, we image in the present study the internal fault zone structures at the Ramona Reservation using local and tele seismic data (Fig. 1) from the two dense arrays RA and RR (Fig. 2). The main aim of this work is to resolve bimaterial interfaces, velocity variations within the fault zone, and properties of the fault damage structures in the study area. The rest of the paper is organized as follows. In the next section we describe the data used for the imaging analyses. The employed techniques and derived results are presented in section 3 and discussed in section 4.

2 Data and preprocessing

Regional tomography results (Allam & Ben-Zion 2012, Allam *et al.* 2014a, Share *et al.* 2019a) suggest the main strand of the SJFZ in the Ramona Reservation, the Clark fault, separates overall faster velocity rocks to the NE from the SW at depth. At this site, two dense arrays (RA and RR in Fig. 2) were installed across three fault surface traces (F1, F2, F3 in Fig. 2) associated with M_w>6 earthquakes in the past 15,000 years (Rockwell *et al.* 2015). The short linear RA array (red balloons in Fig. 2) has 12 three-component strong motion sensors (01 to 12 from SW to NE) over an aperture of ~470 m crossing F2, and started recording in 2012 at 200 samples per second (sps). The RR array contains 65 stations installed along a line with an aperture of ~2.4 km in the fault normal direction (01 to 65 from SW to NE in Fig. 2) and 32 stations distributed around the SW-NE line (Fig. 2) expanding for ~1.4 km in the along fault direction. The RR array has three-component geophones sampling at 500 sps and recorded from Sep 1st to Oct 2nd in 2016. RR stations 28-41 cover a similar area as the RA array. The fault surface traces, F1, F2 and F3, are located between stations RR20-21, RR31-32/RA04-05 and RR42-43, respectively.

We investigate data from 2012-2017 associated with ~180 M>5 teleseismic events (Fig. 1b) with clear P arrivals, and ~42,000 local events within an area (blue box in Fig. 1a) of 200 km in the fault-parallel and 60 km in the fault-normal directions centered on the study site. Of these, ~1700 local and ~11 teleseismic events occurred during the deployment of the RR array. Local P and S wave arrivals are automatically detected (Ross & Ben-Zion 2014, Ross *et al.* 2016), and teleseismic P wave arrivals are estimated using the TauP toolkit (Crotwell *et al.* 1999) and IASP91 velocity model. Seismic recordings are discarded if the signal-to-noise ratio is smaller

124 than 3, defined as the ratio of root-mean-square values between the signal window (e.g. P/S arrivals) and the preceding noise window of the same length.

We first analyze spatial changes of waveforms in the fault normal direction (section 3.1) to identify structural discontinuities. Next, P-wave delay time from teleseismic events, and P-wave relative slowness from local earthquakes within a 60 km $\times$ 20 km box centered on the site (red box in Fig. 1a), are analyzed to investigate local velocity variations (section 3.2). Using the RR array, fault zone head waves (FZHW, section 3.3) from events located <10 km normal to the fault (cyan box in Fig. 1a) are analyzed to constrain bimaterial interface properties (location and velocity contrast). Fault zone trapped waves (FZTW, section 3.4) are investigated to constrain parameters of the core damage zone.

3 Analyses

3.1 Waveform changes

Theoretical results (e.g. Ben-Zion & Aki 1990, Igel *et al.* 1997, Ben-Zion 1998, Jahnke *et al.* 2002) and in-situ observations (e.g. Cormier & Spudich 1984, Rovelli *et al.* 2002, Korneev *et al.* 2003, Catchings *et al.* 2016, Qin *et al.* 2018) show that lateral variations in fault zone structures can affect waveform characteristics, e.g., amplitude, travel time, particle motion and spectral content. We investigate changes in these properties across the RR array using cross-correlation analysis and visual inspection applied to tele and local seismic data. In general, while waveforms change to some extent because of factors such as focal mechanism and event location, there are persistent transitions of waveform characteristics across the three fault surface traces at the study site.

Fig. 3(a) presents 1 Hz lowpass filtered P waves from a teleseismic event (Tele1, labeled in Fig. 1b). We calculate the matrix of cross-correlation coefficients (CC) of the array data in a 2.5 second time window (blue lines in Fig. 3a) starting 0.5 second before the P arrival. The short time window is chosen to suppress the influence of later arrivals. The median CC from all events at RR and RA arrays are presented in Figs. 3(b)&(c). Waveforms at RR stations NE of F3 are highly correlated with each other with CC values close to 1, and less correlated with those from stations to the SW (CC=<0.8). The same pattern emerges for stations between F1 and F3, where the waveforms show high correlation with each other but not with stations outside. There is, however, only a slight decrease in CC values for stations between F2 to F3 compared to those between F1 to F2 (Fig. 3b). This is more clearly seen in the CC results of the short RA array based on more events (Fig. 3c). Fig. 4 displays 1-20 Hz bandpass filtered waveforms of four local events (labeled in Fig. 1a) from four quadrants separated by the local fault-parallel and fault-normal directions. Despite differences in focal mechanisms and locations, we consistently observe changes in phase, amplitude and frequency across stations near the surface traces F1, F2 and F3 (blue, green and red dashed lines in Fig.4). Events with similar waveform change patterns are shown in Fig. 1(a) with yellow stars. The CC patterns and local waveform changes across the arrays imply structural blocks separated by the three fault traces with different material properties that may be related to the fault zone evolution and previous rupture activities.

3.2 Delay time analysis

Following previous studies (e.g. Qiu *et al.* 2017, Share *et al.* 2017), we analyze the arrival time patterns of tele and local seismic P waves to obtain the velocity variations inside the fault zone. Teleseismic waves are lowpass filtered at 1 Hz, and then the delay time for each station relative to the reference station (the SW-most station) in each array is calculated via cross correlation in a 2.5 second time window starting 0.5 second before the P arrival (same time window as in section 3.1). Since the delay times in the two arrays are calculated with respect to different reference stations (RR01 for RR array and RA01 for RA array), only delay time trends in the two arrays are comparable, not the absolute values. Fig. 5(a) presents the delay time from a teleseismic event (location labeled in Fig. 1b, waveforms and time windows shown in Fig. 3a) and the median delay time from all events at RR array. The results indicate a faster NE block relative to the SW, with a broad damage zone that includes areas near the three fault traces. The RA delay time (green dashed line in Fig. 5a) shows consistent results with RR stations over the similar area.

Considering the significant topographic change at the study site (Fig. 2b), we correct the influence of station-event geometry and local topography following Qin *et al.* (2018). The time difference caused by station-event geometry is approximated by the travel time difference predicted from the TauP toolkit (Crotwell *et al.* 1999) and the IASP91 velocity model. Local topography induced delay time is calculated via $dt = (d_i - d_{ref})/v_{ref}$ where d_i and d_{ref} are the elevations of station i and the reference station, and v_{ref} is the reference velocity of the surface layer. We use a reference P-wave velocity here of 4 km/s for the elevation correction. Since station elevation increases from SW to NE, the choice of reference velocity will not affect the general trend that the NE is faster than the SW side; any reasonable velocity used during topography correction will only further decrease the delay on the NE side (Fig. 5) and will not change the major trend of the delay time (see Fig. S1 for results using different reference velocities).

The corrected delay times are shown in Fig. 5(a) as blue (RR array) and red (RA array) dots with error bars representing one standard error. Stations to the NE of F3 are located on a generally faster block compared to the SW side, consistent with the large-scale velocity structure. Stations between RR01 and RR47 have positive relative delay times, indicating an underlying broad damage zone. The maximum delay time is ~0.05 seconds and occurs at stations RR26-31 between F1 and F2, indicating the core of the fault damage zone, which is further elaborated by FZTW analysis in section 3.4. A bimaterial interface with the most significant velocity contrast at the site marks the transition between the broad damage zone and the regionally faster NE block. This interface is imaged in section 3.3 using local FZHW.

For local P wave analysis, we use events that are close to the site (red box in Fig. 1a), and exclude P picks that are more than 1 second away from predicted values using 1D velocity model averaged from the 3D tomographic results of Allam & Ben-Zion (2012). Then we calculate the along-path average slowness using the P-wave travel time divided by the along-path distance, and reject slowness values that are larger than 0.25 s/km or smaller than 0.125 s/km. The relative slowness is obtained as slowness values normalized by the array median value. This procedure was applied at other sites along the SJFZ (Qiu *et al.* 2017, Share *et al.* 2017, Qin *et al.* 2018, Share *et al.* 2019b) and produced stable and reliable relative slowness values within the fault zones irrespective of regional 3D velocity variations. Figs. 5(b)-(d) show relative slowness inside the two arrays and relative slowness histograms from two stations RA01 and RR15. The well-defined median and standard deviation values at each station support the reliability of the obtained relative slowness. The RR results show similar patterns as the teleseismic analysis with the NE side faster than the SW, while the short aperture RA stations show a slightly uniform relative slowness. The RR results exhibit larger variations than those from the RA array because of the limited data available for the RR array. The broad damage zone is less pronounced in Fig. 5(b) as the higher frequency local P arrivals have higher resolution and highlight shallower small-scale variations within the broader damage zone, including very low velocity structures around F2 and stations RR23-27. Ambient noise tomography shows similar variation in shallow S-wave velocity structures contained within a broader low velocity damage zone (Wang *et al.* 2019). More details about the fault damage zone are presented in section 3.4.

3.3 Fault zone head waves

Fault zone head waves (FZHW) are emergent phases that propagate most of their path along a bimaterial interface with the velocity of the faster block and radiate from the interface to the slower side (e.g. Ben-Zion 1990). Synthetic and observed seismograms show that the emergent FZHW have significantly different amplitudes and frequency contents than the impulsive direct P waves (Ben-Zion & Malin 1991; McGuire & Ben-Zion, 2005). FZHW can be used to analyze properties of bimaterial interfaces such as continuity and degree of velocity contrast. The emergent FZHW arrive before the direct impulsive P waves at stations on the slower side closer to the fault than a critical distance x_c defined as $x_c = r \cdot \left(v_2^2/v_1^2 - 1\right)^{\frac{1}{2}}$, where r, v_2, v_1 are the propagation distance along bimaterial interface, P-wave velocity on the fast and slow sides, respectively. The separation time (Δt) between the FZHW and P-wave arrivals decreases when the propagation distance (r) of FZHW along bimaterial interface decreases or the fault normal distance of the station and/or event increases (Share & Ben-Zion 2018), and can be estimated with $\Delta t = r \cdot \Delta v/v^2$ with Δv and v representing, respectively, the differential and average P-wave velocities of the bimaterial interface.

A small critical distance, or fast decay of P-wave and FZHW differential arrival time in the fault normal direction, imply a small velocity contrast or/and short propagation distance of FZHW along bimaterial interface. Different waveform characteristics like motion polarity (e.g. Ben-Zion & Malin 1991, Bulut *et al*. 2012), frequency content (e.g. Share *et al.* 2019b), and arrival time moveout patterns related to the different azimuths of the direct P and FZHW wavefronts are critical to identifying FZHW. Inside the RR array, we observe two types of FZHW: (1) local FZHW (red squares in Fig. 6) related to a local interface between the broad low-velocity damage zone and regionally faster rocks to the NE; (2) regional FZHW (purple squares in Fig. 6) propagating along a deep large scale interface that is connected to the local bimaterial interface.

Fig. 7 presents waveforms from a candidate event (red star in Fig. 6) that generate local FZHW and a reference event nearby (red dot in Fig. 6) that does not. The reference event is likely located too far NE (regional faster side of the SJFZ) at depth to produce critically refracted local FZHW. For stations RR47-26, the first arrivals from the candidate event are emergent with smaller amplitudes compared with those at other stations. From stations RR47 to RR26, the separation time between the first arrivals (i.e. FZHW, green line in Fig. 7a) and direct P waves (red dashed line in Fig. 7a) decreases dramatically from ~0.1 to 0 second. In contrast, the reference event generates impulsive P waves as first arrivals at all stations. In Fig. 7a, the lack of observed FZHW at stations SW of RR26 implies a short propagation distance of FZHW along a bimaterial interface. To confirm this, we present in Fig. 8 the waveforms from all candidate events (red squares in Fig. 6) at stations RR47 with and RR50 without FZHW. Waveforms in Fig. 8 are aligned with the first impulsive P wave arrivals, and plotted with respect to the along-fault-distances of events to the Ramona site. Although the two stations are only ~120 m apart, they are located on different sides of a bimaterial interface, resulting in significantly different first arrivals (i.e. emergent FZHW vs. impulsive P waves). The separation time of FZHW and P waves is 0.1 seconds, and does not change with event distance along the fault, indicating that all these FZHW propagate the same distance along a similar bimaterial patch. Therefore, this type of FZHW is related to a relatively shallow and local bimaterial interface, with structure on the SW of station RR47 being slower than to the NE of that station. Combined with the analysis in sections 3.1-3.2, this local bimaterial interface corresponds to the interface between the broad damage zone and regionally faster block to the NE. A near surface S-wave velocity contrast in a similar location and with the same velocity contrast polarity is observed using ambient noise tomography (Wang *et al.* 2019).

There is also evidence for a deep bimaterial interface that continuously extends from the edge of the broad damage zone down to seismogenic depths. Fig. 9 shows waveforms from a candidate event (purple star in Fig. 6) with FZHW propagating along a deep interface and a reference event nearby (purple dot in Fig. 6). Despite locating also on the regionally slow side of the SJFZ at depth (Allam & Ben-Zion 2012, Share *et al.* 2019a), the reference event is likely too far SW of the deep bimaterial interface and too close to the Ramona site to generate first arriving FZHW (Share & Ben-Zion 2018). The first arrivals from the candidate event at stations RR47-1 are emergent FZHW (green line in Fig. 9a), while the first arrivals from the reference event are impulsive direct P waves. Fig. 10 shows waveforms from all candidate events (purple squares in Fig. 6 in the trifurcation area) at stations RR47 with and RR50 without FZHW. The P waves are delayed by ~0.25 seconds with respect to the FZHW arrivals. This delay is approximately equal for these events given their similar hypocenters. Compared with Figs 7-8, the differential arrival times between P waves and FZHW in Figs 9-10 are generally larger and all stations SW of RR47 record first arriving FZHW (increased critical distance, e.g., Share & Ben-Zion 2018). Especially on the SW of station RR26 where there is no FZHW in Figs 7-8, the P-wave and FZHW differential travel time decreases with a significantly small rate. These observations imply a longer propagation distance of FZHW in Figs 9-10 along a deep bimaterial interface, which connects to the local interface between damage zone and faster NE fault block at the study site. Unfortunately, no other clear FZHW generating events with significantly different hypocentral distances occurred during the month-long RR array deployment. Thus, we are unable to accurately constrain the extent of and velocity contrast across this deep interface. Nevertheless, a deep bimaterial fault that extends continuously from the Clark fault surface trace to seismogenic depth in the trifurcation area is consistent with analysis of FZHW recorded at the Blackburn Saddle site (Fig. 1a, Share *et al.* 2017, Share *et al.* 2019b) and regional scale seismic tomography showing generally faster velocities on the NE side of the Clark fault (Allam *et al.* 2014a).

Despite the poor constraints on P velocity properties of the regional bimaterial interface at depth, we are able to use the azimuthal and frequency differences between the FZHW and direct P waves to constrain the properties of the bimaterial interface near the surface. This is done using beamforming (e.g. Rost & Thomas 2002) over azimuth, horizontal slowness and frequency space to separate coherent FZHW (lower frequency) from coherent direct P waves (higher frequency). For beamforming, we only use stations SW of the bimaterial interface (SW of RR47), inside the broader damage zone defined in Fig. 5(a) and only a selection of stations along the main across-fault profile. Stations for beamforming analysis are plotted with green balloons in Fig. 2(a). This allows the best beamforming results using stations that (1) all record FZHW, (2) all locate within similar velocity structure (even though the velocity is lowest), (3) are more homogeneously spaced and (4) have comparable elevations relative to the array aperture (all selected stations are within 40 m elevation of the central station – RR34).

We systematically search slowness space from 0.03 to 0.43 s/km in increments of 0.01 s/km, azimuth space from 0 to 360 in 1 degree increments and frequency space from 2 to 19 Hz in steps of 1 Hz with a bandwidth of +/- 1 Hz at each step. For each combination of slowness, azimuth and frequency, beamforming is done on 2 seconds P waveforms (starting 0.5 s before first arrival) using a 4-th root slant slack (Rost & Thomas 2002) to capture as best as possible the weak FZHW signals. The beamforming results applied to the candidate event in Fig. 9(a) are shown in Fig. 11. Similar results are obtained for the other candidate events in Fig. 8(a) (not shown). The centers of the two most pronounced beams, and therefore coherent plane wavefronts, are associated with parameters s=0.14 km/s, azimuth=100 degrees and central frequency=5 Hz (Fig. 11a), and s=0.17 km/s, azimuth=152 degrees and central frequency=13 Hz (Fig. 11b). These represent respectively the FZHW wavefront propagating from the fault (lower dominant frequency) and the direct P wavefront originating from the event epicenter (higher dominant frequency). Due to the irregular geometry of the array stations employed in beamforming, some quantification of uncertainty in these estimates is required. Array transfer function for the 4-6 Hz and 12-14 Hz frequency ranges (Fig. S2a & b) show faint artefacts are present in the across-fault (azimuth=40°) and along-fault (azimuth=130°) directions, because of the two main array profile azimuths. The average radii of the central beams in these plots are 0.1 s/km (4-6 Hz) and 0.04 s/km (12-14 Hz) (Fig. S2). However, neither the obtained FZHW nor direct P beams are close to the 40°, 130° azimuths so we consider them well constrained to within a slowness error of 0.04-0.1 s/km.

Using the obtained FZHW and direct P parameters, we slant stack the respective traces (4-th root modulation not applied), cross correlate the resultant beam trace with each individual trace allowing only a time shift equal to the dominant period for that phase (1/5 s = FZHW and 1/13 s = direct P), and then stack the highest correlating traces again. This allows the best quality coherent beam trace in the presence of complex fault zone structures and an uneven surface. The final stacked beam traces at the location of station RR34 shows the earlier arrival of the FZHW wavefront (red) compared to the direct P wavefront (black) (Fig. 11c). The time difference between FZHW and direct P waves is reduced compared to station RR47 (Fig. 8a) as RR34 is farther from the bimaterial interface. The horizontal particle motions of the beam traces (Fig. 11d) highlight again the FZHW radiating from the fault (red particles) and direct P waves pointing to the event epicenter (black particles). The deviation in azimuth obtained from beamforming and horizontal particle motions for the high frequency direct P waves (Fig. 11d) probably relates to the interactions of the respective wavefronts with the free surface, and may also indicate anisotropic velocity structure within the broad damage zone (Bear *et al.* 1999, Li *et al.* 2015). Using the more robust estimate of FZHW azimuth from beamforming (Fig. 11a), we estimate an apparent velocity contrast across the interface around RR47. Given the surface fault strike of 130 degrees (FZHW propagate along fault surface on fast side) and a FZHW azimuth of 100 degrees in the SW, using Snell's Law the apparent velocity contrast relative to the NE block is 13.4%. This is an apparent estimate because it doesn't consider potential dipping fault geometry and the incident angles of the respective P phases.

3.4 Fault zone trapped waves

Fault zone trapped waves (FZTW) are critically reflected phases that constructively interfere inside a low-velocity zone such as fault related core damage zone (e.g. Ben-Zion & Aki 1990, Ben-Zion 1998). The most common type of FZTW, Love-type SH signals following the direct *S* arrival, have been observed in many places (e.g., Li *et al.* 1990, 1994, 1997, Ben-Zion *et al.* 2003, Haberland *et al.* 2003, Mamada *et al.* 2004, Mizuno & Nishigami 2006, Cochran *et al.* 2009, Lewis & Ben-Zion 2010). A less common type of trapped waves involving leaky modes between the *P* and *S* body waves is also generated in some cases (Malin *et al.* 2006, Gulley *et al.* 2017). Both types of FZTW have been observed in previous studies along the SJFZ (e.g. Qiu *et al.* 2017, Qin *et al.* 2018). Events that generate FZTW inside the RR array are shown as green squares in Fig. 1(a). These events are selected using the automatic picking algorithm (Ross & Ben-Zion 2015) and confirmed based on visual inspection. Fig. 12 presents the vertical and fault parallel waveforms from a candidate event (TW1, labeled in Fig. 1a) containing large amplitude wave packages related to P- and S- type FZTW (red dashed boxes in Fig. 12). The locations of stations recording FZTW (RR26-31) are consistent with the lowest velocity zone (maximum delay) obtained from delay time analysis (section 3.2, Fig. 5).

We next model the observed Love-type FZTW using the 2D analytic solution of Ben-Zion & Aki (1990), and invert for properties of the core damage zone with a genetic inversion algorithm (e.g. Ben-Zion *et al.* 2003, Qiu *et al.* 2017, Share *et al.* 2017). We use a three-layer fault zone model with a low velocity zone sandwiched between two half spaces, and describe the model with six parameters: shear wave velocities of the half space and damage zone, and, Q value, width, depth, and location of the SW edge of the damage zone. Though the study site has quite complex structures based on the analyses in sections 3.1-3.3, adding more parameters will greatly increase the null space of the inversion and the possibility of ending up with local minima. Therefore, this simplified three-layer six parameter model provides a useful approach because it encompasses the key average properties affecting FZTW in the core damage zone, while accounting analytically for the significant trade-offs between model parameters (Ben-Zion 1998).

Fig. 13 shows the fitness values (green dots in Fig. 13a) for the six model parameters and waveform fit for the candidate event in Fig. 12. The black curves in Fig. 13(a) represent the probability density functions obtained by summing the fitness values for the final 2000 models during inversion. The black dots in Fig. 13(a) shows the best-fitting model that generates the synthetic waveforms in Fig. 13(b), which are close to the probability density distribution peaks, i.e. the most likely model. Both the phase and amplitude of FZTW from the best fitting model are similar to the observed FZTW (Fig. 13b). The large fitness values (>0.7) and narrow peaks of the probability density functions, and, the good fit between the best-fitting and most likely models imply robust inversion results. Combined with the modeling results from another event (Fig. S3, Supporting Information), the obtained core damage zone is ~100 m wide and ~4 km deep, with Q value of ~20 and 40% S-wave velocity reduction compared with the host rock with S-wave velocity of ~3.2 km/s, consistent with the analyses in sections 3.1-3.3. The FZTW results pinpoint the location, depth extent and other parameters of a core damage zone that lies within the flower-shaped broader damage zone at the site (Wang *et al.* 2019).

4 Discussion and Conclusions

This study uses various fault zone phases and analysis techniques to provide collectively high-resolution images for the SJFZ at the Ramona Reservation, north of Anza, California. Fig. 14 presents a schematic local velocity model based on the study. Delay times (section 3.2) from tele and local seismic data indicate a faster NE side than the SW, with the major velocity contrast close to station RR47 separating the regionally NE faster block from a broad low velocity damage zone. This velocity contrast is also the interface from which local and regional FZHW (section 3.3) refract before being recorded at SW stations, and, is consistent with the waveform changes (section 3.1) across the local fault surface trace F3. The core damage zone beneath stations RR26-31 (i.e. between the local fault surface traces F1 and F2 related to the observed waveform changes in section 3.1) causes the most significant P-wave delays (0.05 second; Fig. 5a) inside the array and generates P- and S- type FZTW (section 3.4). Modeling of S-type FZTW indicates that the core damage zone is ~100 m wide ~4 km deep and has Q value of 20 and 40% S-wave velocity reduction compared with the host rock with S-wave velocity of 3.2 km/s.

Assuming that the local bimaterial interface around RR47 also extends to ~4 km depth and the local FZHW propagate near-vertically along most of that length, the ~0.1 second differential time between FZHW and direct P waves observed at RR47 (Fig. 8a) corresponds to a velocity contrast of ~12% for a NE-side P-wave velocity of 5.6 km/s (1.75x3.2 km/s). This is consistent with the apparent contrast of 13.4% in section 3.3 and lie within the 11-23% P velocity contrast range for the deep bimaterial SJFZ ~10 km to the NW (Share *et al.* 2019b).

The analyses of different data sets (e.g. teleseismic and local seismic data, travel time and azimuth) also resolve structures at different scales. The teleseismic waves have almost identical paths before arriving at the stations, thus the delay time patterns are indicative of the shallow structure beneath the array with NE side faster than the SW and a core damage zone beneath stations RR26-31. The observed fault damage zone is compatible with waveform modeling results based on FZTW. Relative slowness analysis of local seismic data uses along-path average slowness and can be affected by both regional (e.g. bimaterial interface) and local (e.g. local damage zones) structures. Previous large-scale imaging results suggest that the velocity contrast at the Ramona Reservation is as large as 20% and very well confined (Allam & Ben-Zion 2012), therefore the large-scale velocity structure plays a major role in affecting the along-path average slowness. The relative slowness study shows a velocity contrast with NE of station RR47 faster than the SW, consistent with the bimaterial interface properties from FZHW analyses. However, it does not resolve the local fault damage zone, because the core damage zone is highly confined (~100 m wide in section 3.4) and the broad damage zone concentrates in the shallow structure. All the obtained results consistently imply faster velocity on the NE side with a core damage structure between F1 and F2 embedded within a broader flower-shape damage zone at the study site. Accounting for the imaged bimaterial interfaces and local damage zones can improve the accuracy of earthquake locations with respect to the fault, focal mechanisms, receiver function results and local body wave tomography models (e.g., McNally & McEvilly 1977, Ben-Zion & Malin 1991, Schulte-Pelkum & Ben-Zion 2012, Bennington *et al.* 2013).

Large-scale imaging of the region around the central SJFZ (e.g., Allam & Ben-Zion 2012, Zigone *et al.* 2015) show that the NE block in the study area is faster than the SW. Detailed linear array studies along the SJFZ (Qiu *et al.* 2017, Share *et al.* 2017, Qin *et al.* 2018, Share *et al.* 2019b) consistently indicate such a regional bimaterial interface polarity (Fig. S4). For right-lateral loading, this velocity contrast can produce a statistically preferred rupture propagation direction to the NW (Andrews & Ben-Zion 1997, Shi & Ben-Zion 2006, Brietzke *et al.* 2009). This theoretical expectation is supported by observational studies of directivity of small earthquakes in the region (Kurzon *et al.* 2014, Ross & Ben-Zion 2016, Meng *et al.* 2020). Repeated rupture with preferred propagation direction will generate damaged material on the faster side of the fault (Ben-Zion & Shi 2005, Xu *et al.* 2012). Such damage zones are observed at various sites (BB, SGB, JF) on the NE side of the SJFZ based on analysis of FZTW. Modeling of FZTW at BB, SGB and JF sites along the SJFZ suggests narrow (~70-200 m wide) core damage zones with significant 30-60 % S-wave velocity reductions and Q values of 20-60 in the top 2-5 km. Severely damaged structures at the SGB site cause local reversals of the large-scale velocity contrast, complicating the internal fault structures. Local FZHW further validate the existence of bimaterial interfaces and damage zones, observed at the JF and BB sites on the SW of the interface between local damage zones and the faster NE fault block (Fig. S4).

Similar bimaterial interfaces and damage structures illuminated by various fault zone phases were observed at other large fault systems. FZHW were used to image deep velocity contrasts along the Hayward fault (Allam *et al*. 2014b), the North Anatolian fault (Bulut *et al.* 2012) and various sections of the San Andreas fault (McGuire & Ben-Zion 2005, Lewis *et al.* 2007, Zhao *et al.* 2010). FZTW were observed along the North Anatolian fault (Ben-Zion *et al.* 2003), the San Andreas fault (e.g. Li *et al*. 1990, Lewis & Ben-Zion 2010), Japan (e.g. Mamada *et al*. 2004, Mizuno & Nishigami 2006), Italy (e.g. Rovelli *et al*. 2002), Israel (Haberland *et al*. 2003) and other locations. The observed core damage structures are usually 100-200 m wide and concentrate in the top 2-4 km with 20-40 % S-wave velocity reductions. The resulting high-resolution images of the internal fault zone features provide important information for understanding persistent properties of local earthquake ruptures, and improve the accuracy of derived earthquake locations, focal mechanisms and more.

The Ramona Reservation site is characterized by three fault surface traces separating different materials with a core damage zone surrounded by a broad shallow damage structure. Multiple historic ruptures of moderate and large earthquakes in the Ramona Reservation area altered the local velocity structure and produced rock damage asymmetry with more damage on the faster side of the main fault (Dor *et al.* 2006). The most recent rupture in 1918 at this site was located on a fault trace SW of F1 (Rockwell *et al.* 2015), and probably has contributed to the observed damage zone in this study on the NE side of the ruptured trace. Studies at other sites along the SJFZ (Qiu *et al.* 2017, Share *et al.* 2017, Qin *et al.* 2018, Share *et al.* 2019b) consistently resolve bimaterial interfaces separating faster blocks to the NE and asymmetric damage zones in corroboration with the preferred propagation direction of large earthquakes in the central section of the SJFZ to the NW. This increases the seismic shaking hazard in the large communities to the NW of Anza, CA.

5 Acknowledgements

The paper benefitted from useful comments by Christian Haberland, an anonymous referee and Editor Ana Ferreira. The study was supported by the U.S. Department of Energy (awards DE-SC0016520 and DE-SC0016527).

References

Allam, A.A. & Ben-Zion, Y. (2012) Seismic velocity structures in the southern California plate-boundary environment from double-difference tomography. *Geophys. J. Int.*, **190**, 1181–1196. doi:10.1111/j.1365-246X.2012.05544.x

Allam, A.A., Ben-Zion, Y., Kurzon, I. & Vernon, F.L. (2014a) Seismic velocity structure in the Hot Springs and Trifurcation areas of the San Jacinto fault zone, California, from double-difference tomography. *Geophys. J. Int.*, **198**, 978–999. doi:10.1093/gji/ggu176

Allam, A.A., Ben-Zion, Y. & Peng, Z. (2014b) Seismic Imaging of a Bimaterial Interface Along the Hayward Fault, CA, with Fault Zone Head Waves and Direct P Arrivals. *Pure Appl. Geophys.*, **171**, 2993–3011. doi:10.1007/s00024-014-0784-0

Andrews, D.J. & Ben-Zion, Y. (1997) Wrinkle-like slip pulse on a fault between different materials. *J. Geophys. Res.*, **102**, 553–571.

Bear, L.K., Pavlis, G.L. & Bokelmann, G.H.R. (1999) Multi-wavelet analysis of three-component seismic arrays: Application to measure effective anisotropy at Pinon Flats, California. *Bull. Seismol. Soc. Am.*, **89**, 693–705.

Becker, T.W., Hardebeck, J.L. & Anderson, G. (2005) Constraints on fault slip rates of the southern California plate boundary from GPS velocity and stress inversions. *Geophys. J. Int.*, **160**, 634–650. doi:10.1111/j.1365-246X.2004.02528.x

Ben-Zion, Y. (1990) The response of two half spaces to point dislocations at the material interface. *Geophys. J. Int.*, **101**, 507–528. doi:10.1111/j.1365-246X.1990.tb05567.x

Ben-Zion, Y. (1998) Properties of seismic fault zone waves and their utility for imaging low-velocity structures. *J. Geophys. Res. Solid Earth*, **103**, 12567–12585. doi:10.1029/98jb00768

Ben-Zion, Y. (2001) Dynamic ruptures in recent models of earthquake faults. *J. Mech. Phys. Solids*, **49**, 2209–2244. doi:10.1016/S0022-5096(01)00036-9

Ben-Zion, Y. & Aki, K. (1990) Seismic radiation from an SH line source in a laterally heterogeneous planar fault zone. *Bull. - Seismol. Soc. Am.*, **80**, 971–994.

Ben-Zion, Y. & Malin, P. (1991) San Andreas Fault Zone Head Waves Near Parkfield , California. *Science (80-.).*, **251**, 1592–1594. Retrieved from https://www.jstor.org/stable/2875727

Ben-Zion, Y., Peng, Z., Okaya, D., Seeber, L., Armbruster, J.G., Ozer, N., Michael, A.J., *et al.* (2003) A shallow fault-zone structure illuminated by trapped waves in the Karadere-Duzce branch of the North Anatolian Fault, western Turkey. *Geophys. J. Int.*, **152**, 699–717. doi:10.1046/j.1365-246X.2003.01870.x

Ben-Zion, Y. & Sammis, C.G. (2003) Characterization of Fault Zones. *Pure Appl. Geophys.*, **160**, 677–715.

Ben-Zion, Y. & Shi, Z. (2005) Dynamic rupture on a material interface with spontaneous generation of plastic strain in the bulk. *Earth Planet. Sci. Lett.*, **236**, 486–496. doi:10.1016/j.epsl.2005.03.025

Ben-Zion, Y. *et al.* (2015) Basic data features and results from a spatially dense seismic array on the San Jacinto fault zone, *Geophys. J. Int.,* **202**(1), 370–380

Bennington, N.L., Thurber, C., Peng, Z., Zhang, H. & Zhao, P. (2013) Incorporating fault zone head wave and direct wave secondary arrival times into seismic tomography: Application at Parkfield, California. *J. Geophys. Res. Solid Earth*, **118**, 1008–1014. doi:10.1002/jgrb.50072

Brietzke, G.B., Cochard, A. & Igel, H. (2009) Importance of bimaterial interfaces for earthquake dynamics and strong ground motion. *Geophys. J. Int.*, **178**, 921–938. doi:10.1111/j.1365-246X.2009.04209.x

Bulut, F., Ben-Zion, Y. & Bohnhoff, M. (2012) Evidence for a bimaterial interface along the Mudurnu segment of the North Anatolian Fault Zone from polarization analysis of P waves. *Earth Planet. Sci. Lett.*, **327–328**, 17–22, Elsevier B.V. doi:10.1016/j.epsl.2012.02.001

Catchings, R.D., Goldman, M.R., Li, Y.-G. & Chan, J.H. (2016) Continuity of the west napa-franklin fault zone inferred from guided waves generated by earthquakes following the 24 august 2014 Mw 6.0 south napa earthquake. *Bull. Seismol. Soc. Am.*, **106**, 2721–2746. doi:10.1785/0120160154

Cochran, E.S., Li, Y.-G., Shearer, P.M., Barbot, S., Fialko, Y. & Vidale, J.E. (2009) Seismic and geodetic evidence for extensive, long-lived fault damage zones. *Geology*, **37**, 315–318. doi:10.1130/G25306A.1

Cormier, V.F. & Spudich, P. (1984) Amplification of ground motion and waveform complexity in fault zones: examples from the San Andreas and Calaveras Faults. *Geophys. J. R.*, **79**, 135–152.

Crotwell, H.P., Owens, T.J. & Ritsema, J. (1999) The TauP Toolkit : Flexible Seismic Travel-time and Ray-path Utilities. *Seismol. Res. Lett.*, **70**, 154–160.

Dor, O., Rockwell, T.K. & Ben-Zion, Y. (2006) Geological observations of damage asymmetry in the structure of the San Jacinto, San Andreas and Punchbowl faults in Southern California: A possible indicator for preferred rupture propagation direction. *Pure Appl. Geophys.*, **163**, 301–349. doi:10.1007/s00024-005-0023-9

Fay, N.P. & Humphreys, E.D. (2005) Fault slip rates, effects of elastic heterogeneity on geodetic data, and the strength of the lower crust in the Salton Trough region, southern California. *J. Geophys. Res. Solid Earth*, **110**, 1–14. doi:10.1029/2004JB003548

Gulley, A.K., Kaipio, J.P., Eccles, J.D. & Malin, P.E. (2017) A numerical approach for modelling fault-zone trapped waves. *Geophys. J. Int.*, **210**, 919–930. doi:10.1093/gji/ggx199

Haberland, C., Agnon, A., El-Kelani, R., Maercklin, N., Qabbani, I., Rümpker, G., Ryberg, T., *et al.* (2003) Modeling of seismic guided waves at the Dead Sea Transform. *J. Geophys. Res. Solid Earth*, **108**. doi:10.1029/2002jb002309

Hauksson, E., Yang, W. & Shearer, P.M. (2012) Waveform relocated earthquake catalog for Southern California (1981 to June 2011). *Bull. Seismol. Soc. Am.*, **102**, 2239–2244. doi:10.1785/0120120010

Harjes, H.-P. & Henger, M. (1973): Array-Seismology. Zeitsch. f. Geophysik. 39, S. 865-905

Igel, H., Ben-Zion, Y. & Leary, P.C. (1997) Simulation of SH- and P-SV-wave propagation in fault zones. *Geophys. J. Int.*, **128**, 533–546. doi:10.1111/j.1365-246X.1997.tb05316.x

Jahnke, G., Igel, H. & Ben-Zion, Y. (2002) Three-dimensional calculations of fault-zone-guided waves in various irregular structures. *Geophys. J. Int.*, **151**, 416–426. doi:10.1046/j.1365-246X.2002.01784.x

Korneev, V.A., Nadeau, R.M. & McEvilly, T. V. (2003) Seismological studies at Parkfield IX: Fault-zone imaging using guided wave attenuation. *Bull. Seismol. Soc. Am.*, **93**, 1415–1426. doi:10.1785/0120020114

Kurzon, I., Vernon, F.L., Ben-Zion, Y. & Atkinson, G. (2014) Ground Motion Prediction Equations in the San Jacinto Fault Zone: Significant Effects of Rupture Directivity and Fault Zone Amplification. *Pure Appl. Geophys.*, **171**, 3045–3081. doi:10.1007/s00024-014-0855-2

Lewis, M.A. & Ben-Zion, Y. (2010) Diversity of fault zone damage and trapping structures in the Parkfield section of the San Andreas Fault from comprehensive analysis of near fault seismograms. *Geophys. J. Int.*, **183**, 1579–1595. doi:10.1111/j.1365-246X.2010.04816.x

Lewis, M.A., Ben-Zion, Y. & McGuire, J.J. (2007) Imaging the deep structure of the San Andreas Fault south of Hollister with joint analysis of fault zone head and direct P arrivals. *Geophys. J. Int.*, **169**, 1028–1042. doi:10.1111/j.1365-246X.2006.03319.x

Lewis, M.A., Peng, Z., Ben-Zion, Y. & Vernon, F.L. (2005) Shallow seismic trapping structure in the San Jacinto fault zone near Anza, California. *Geophys. J. Int.*, **162**, 867–881. doi:10.1111/j.1365-246X.2005.02684.x

Li, Y.-G., Aki, K., Adams, D., Hasemi, A. & Lee, W.H.K. (1994) Seismic guided waves trapped in the fault zone of the Landers, California, earthquake of 1992. *J. Geophys. Res.*, **99**. doi:10.1029/94jb00464

Li, Y.-G., Ellsworth, W.L., Thurber, C.H., Malin, P.E. & Aki, K. (1997) Fault-zone guided waves from explosions in the San Andreas fault at Parkfield and Cienega Valley, California. *Bull. Seismol. Soc. Am.*, **87**, 210–221.

Li, Y.-G., Leary, P., Aki, K. & Malin, P. (1990) Seismic Trapped Modes in the Oroville and San Andreas Fault Zones, **249**, 763–766. Retrieved from https://www.jstor.org/stable/2878078

Li, Z., Peng, Z., Ben-Zion, Y. & Vernon, F.L. (2015) Spatial variations of shear wave anisotropy near the San Jacinto Fault Zone in Southern California. *J. Geophys. Res. Solid Earth*, **120**, 8334–8347. doi:10.1002/2015JB012483

Lindsey, E.O. & Fialko, Y. (2013) Geodetic slip rates in the southern San Andreas Fault system:

Effects of elastic heterogeneity and fault geometry. *J. Geophys. Res. Solid Earth*, **118**, 689–697. doi:10.1029/2012JB009358

Malin, P., Shalev, E., Balven, H. & Lewis-Kenedi, C. (2006) Structure of the San Andreas Fault at SAFOD from P-wave tomography and fault-guided wave mapping. *Geophys. Res. Lett.*, **33**, 3–5. doi:10.1029/2006GL025973

Mamada, Y., Kuwahara, Y., Ito, H. & Takenaka, H. (2004) Discontinuity of the Mozumi-Sukenobu fault low-velocity zone, central Japan, inferred from 3-D finite-difference simulation of fault zone waves excited by explosive sources. *Tectonophysics*, **378**, 209–222. doi:10.1016/j.tecto.2003.09.008

McGuire, J. & Ben-Zion, Y. (2005) High-resolution imaging of the Bear Valley section of the San Andreas fault at seismogenic depths with fault-zone head waves and relocated seismicity. *Geophys. J. Int.*, **163**, 152–164. doi:10.1111/j.1365-246X.2005.02703.x

McNally, K.C. & McEvilly, T. V. (1977) Velocity contast across the San Andreas fault in central California: small-scale variations from P-wave nodal plane distortion. *Bull. Seismol. Soc. Am.*, **67**, 1565–1576.

Meng, H., McGuire, J.J. & Ben-Zion, Y. (2020) Semi-Automated Estimates of Directivity and Related Source Properties of Small to Moderate Southern California Earthquakes using Second Seismic Moments. *J. Geophys. Res. Solid Earth*, **125**, 1–21. doi:10.1029/2019jb018566

Mitchell, T.M., Ben-Zion, Y. & Shimamoto, T. (2011) Pulverized fault rocks and damage asymmetry along the Arima-Takatsuki Tectonic Line, Japan. *Earth Planet. Sci. Lett.*, **308**, 284–297, Elsevier B.V. doi:10.1016/j.epsl.2011.04.023

Mizuno, T. & Nishigami, K.Y. (2006) Deep structure of the Nojima Fault, southwest Japan, estimated from borehole observations of fault-zone trapped waves. *Tectonophysics*, **417**, 231–247. doi:10.1016/j.tecto.2006.01.003

Onderdonk, N.W., Rockwell, T.K., Mcgill, S.F. & Marliyani, G.I. (2013) Evidence for seven surface ruptures in the past 1600 years on the claremont fault at mystic lake, northern san jacinto fault zone, California. *Bull. Seismol. Soc. Am.*, **103**, 519–541. doi:10.1785/0120120060

Peng, Z., Ben-Zion, Y., Michael, A.J. & Zhu, L. (2003) Quantitative analysis of seismic fault zone waves in the rupture zone of the 1992 Landers, California, earthquake: Evidence for a shallow trapping structure. *Geophys. J. Int.*, **155**, 1021–1041. doi:10.1111/j.1365-246X.2003.02109.x

Petersen, M.D. & Wesnousky, S.G. (1994) Fault slip rates and earthquake histories for active faults in southern California. *Bull. Seismol. Soc. Am.*, **84**, 1608–1649.

Qin, L., Ben-Zion, Y., Qiu, H., Share, P.-E., Ross, Z.E. & Vernon, F.L. (2018) Internal structure of the san jacinto fault zone in the trifurcation area southeast of anza, california, from data of dense seismic arrays. *Geophys. J. Int.*, **213**, 98–114. doi:10.1093/gji/ggx540

Qiu, H., Ben-Zion, Y., Ross, Z.E., Share, P.-E. & Vernon, F.L. (2017) Internal structure of the San Jacinto fault zone at Jackass Flat from data recorded by a dense linear array. *Geophys. J. Int.*, **209**, 1369–1388. doi:10.1093/gji/ggx096

Rockwell, T.K., Dawson, T.E., Young Ben-Horin, J. & Seitz, G. (2015) A 21-Event, 4,000-Year History of Surface Ruptures in the Anza Seismic Gap, San Jacinto Fault, and Implications for Long-term Earthquake Production on a Major Plate Boundary Fault. *Pure Appl. Geophys.*, **172**, 1143–1165. doi:10.1007/s00024-014-0955-z

Ross, Z.E. & Ben-Zion, Y. (2014) Automatic picking of direct P, S seismic phases and fault zone head waves. *Geophys. J. Int.*, **199**, 368–381. doi:10.1093/gji/ggu267

Ross, Z.E. & Ben-Zion, Y. (2015) An algorithm for automated identification of fault zone trapped waves. *Geophys. J. Int.*, **202**, 933–942. doi:10.1093/gji/ggv197

Ross, Z.E. & Ben-Zion, Y. (2016) Toward reliable automated estimates of earthquake source properties from body wave spectra. *J. Geophys. Res. Solid Earth*, **121**, 4390–4407. doi:10.1002/2016JB013003

Ross, Z.E., Hauksson, E. & Ben-Zion, Y. (2017) Abundant off-fault seismicity and orthogonal structures in the San Jacinto fault zone. *Sci. Adv.*, **3**. doi:10.1126/sciadv.1601946

Ross, Z.E., White, M.C., Vernon, F.L. & Ben-Zion, Y. (2016) An improved algorithm for real-time s-wave picking with application to the (Augmented) anza network in Southern California. *Bull. Seismol. Soc. Am.*, **106**, 2013–2022. doi:10.1785/0120150230

Rost, S. & Thomas, C. (2002) Array seismology: Methods and applications. *Rev. Geophys.*, **40**, 2-1-2–27. doi:10.1029/2000RG000100

Rovelli, A., Caserta, A., Marra, F. & Ruggiero, V. (2002) Can seismic waves be trapped inside an inactive fault zone? The case study of Nocera Umbra, Central Italy. *Bull. Seismol. Soc. Am.*, **92**, 2217–2232. doi:10.1785/0120010288

Salisbury, J.B., Rockwell, T.K., Middleton, T.J. & Hudnut, K.W. (2012) LiDAR and field observations of slip distribution for the most recent surface ruptures along the central san Jacinto fault. *Bull. Seismol. Soc. Am.*, **102**, 598–619. doi:10.1785/0120110068

Schulte-Pelkum, V. & Ben-Zion, Y. (2012) Apparent vertical Moho offsets under continental strike-slip faults from lithology contrasts in the seismogenic crust. *Bull. Seismol. Soc. Am.*, **102**, 2757–2763. doi:10.1785/0120120139

Share, P.-E., Allam, A.A., Ben-Zion, Y., Lin, F.C. & Vernon, F.L. (2019b) Structural Properties of the San Jacinto Fault Zone at Blackburn Saddle from Seismic Data of a Dense Linear Array. *Pure Appl. Geophys.*, **176**, 1169–1191. doi:10.1007/s00024-018-1988-5

Share, P.-E. & Ben-Zion, Y. (2018) A Bimaterial Interface Along the Northern San Jacinto Fault Through Cajon Pass. *Geophys. Res. Lett.*, **45**, 11,622-11,631. doi:10.1029/2018GL079834

Share, P.-E., Ben-Zion, Y., Ross, Z.E., Qiu, H. & Vernon, F.L. (2017) Internal structure of the San Jacinto fault zone at Blackburn Saddle from seismic data of a linear array. *Geophys. J. Int.*, **210**, 819–832. doi:10.1093/gji/ggx191

Share, P.-E., Guo, H., Thurber, C.H., Zhang, H. & Ben-Zion, Y. (2019a) Seismic Imaging of the Southern California Plate Boundary around the South-Central Transverse Ranges Using Double-Difference Tomography. *Pure Appl. Geophys.*, **176**, 1117–1143. doi:https://doi.org/10.1007/s00024-018-2042-3

Shi, Z. & Ben-Zion, Y. (2006) Dynamic rupture on a bimaterial interface governed by slip-weakening friction. *Geophys. J. Int.*, **165**, 469–484. doi:10.1111/j.1365-246X.2006.02853.x

Shlomai, H. & Fineberg, J. (2016) The structure of slip-pulses and supershear ruptures driving slip in bimaterial friction. *Nat. Commun.*, **7**, 1–7, Nature Publishing Group. doi:10.1038/ncomms11787

Wang, Y., Allam, A.A. & Lin, F.C. (2019) Imaging the Fault Damage Zone of the San Jacinto Fault Near Anza With Ambient Noise Tomography Using a Dense Nodal Array. *Geophys. Res. Lett.*, **46**, 12938–12948. doi:10.1029/2019GL084835

Weertman, J. (1980) Unstable slippage across a fault that separates elastic media of different elastic constants. *J. Geophys. Res.*, **85**, 1455–1461.

Xu, S. & Ben-Zion, Y. (2017) Theoretical constraints on dynamic pulverization of fault zone rocks. *Geophys. J. Int.*, **209**, 282–296. doi:10.1093/gji/ggx033

Xu, S., Ben-Zion, Y. & Ampuero, J.P. (2012) Properties of inelastic yielding zones generated by in-plane dynamic ruptures-II. Detailed parameter-space study. *Geophys. J. Int.*, **191**, 1343–1360. doi:10.1111/j.1365-246X.2012.05685.x

Zhao, P., Peng, Z., Shi, Z., Lewis, M.A. & Ben-Zion, Y. (2010) Variations of the velocity contrast and rupture properties of M6 earthquakes along the Parkfield section of the San Andreas fault. *Geophys. J. Int.*, **180**, 765–780. doi:10.1111/j.1365-246X.2009.04436.x

Zigone, D., Ben-Zion, Y., Campillo, M. & Roux, P. (2015) Seismic Tomography of the Southern California Plate Boundary Region from Noise-Based Rayleigh and Love Waves. *Pure Appl. Geophys.*, **172**, 1007–1032. doi:10.1007/s00024-014-0872-1

Zigone, D., Ben-Zion, Y., Lehujeur, M., Campillo, M., Hillers, G. & Vernon, F.L. (2019) Imaging subsurface structures in the San Jacinto fault zone with high-frequency noise recorded by dense linear arrays. *Geophys. J. Int.*, **217**, 879–893, Oxford University Press. doi:10.1093/gji/ggz069

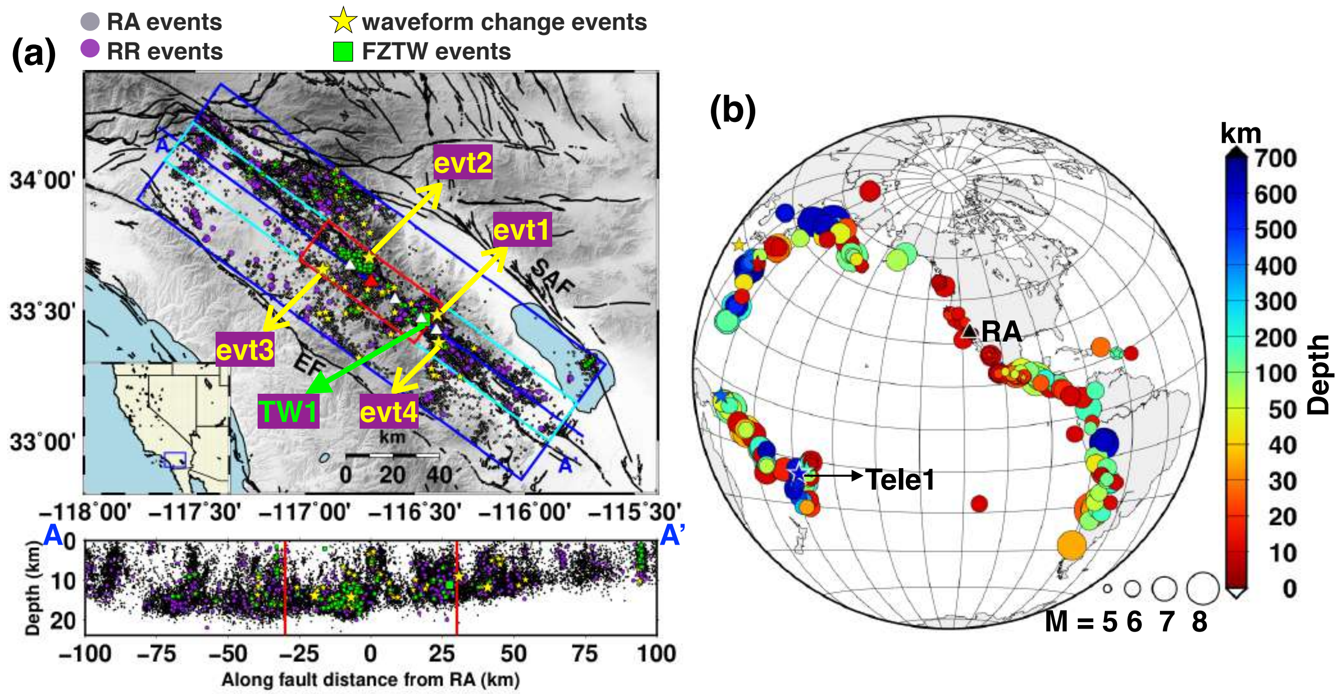

Figure 1. (a). All local events recorded by the short RA and long RR arrays. Lower panel shows the depth profile projected to AA'. The Ramona site is shown as a red triangle, and other four linear arrays along the SJFZ (BB, SGB, DW, JF from NW to SE) are plotted with white triangles. The blue, cyan, and red boxes define the areas where we search for FZTW and waveform changes, FZHW, and perform delay time analysis of local earthquakes, respectively. The four labeled events (evt 1-4; big yellow stars) are examples for waveform change study (Fig. 4), and TW1 (big green square) is the FZTW candidate event (Figs 12-13). (b). All teleseismic events in 2012-2017 that are used in the short RA (circles) and long RR (stars) array studies. Color represents event depth and circle size indicates event magnitude. The RA site (black triangle) and example event Tele1 (Fig. 3) are outlined in white.

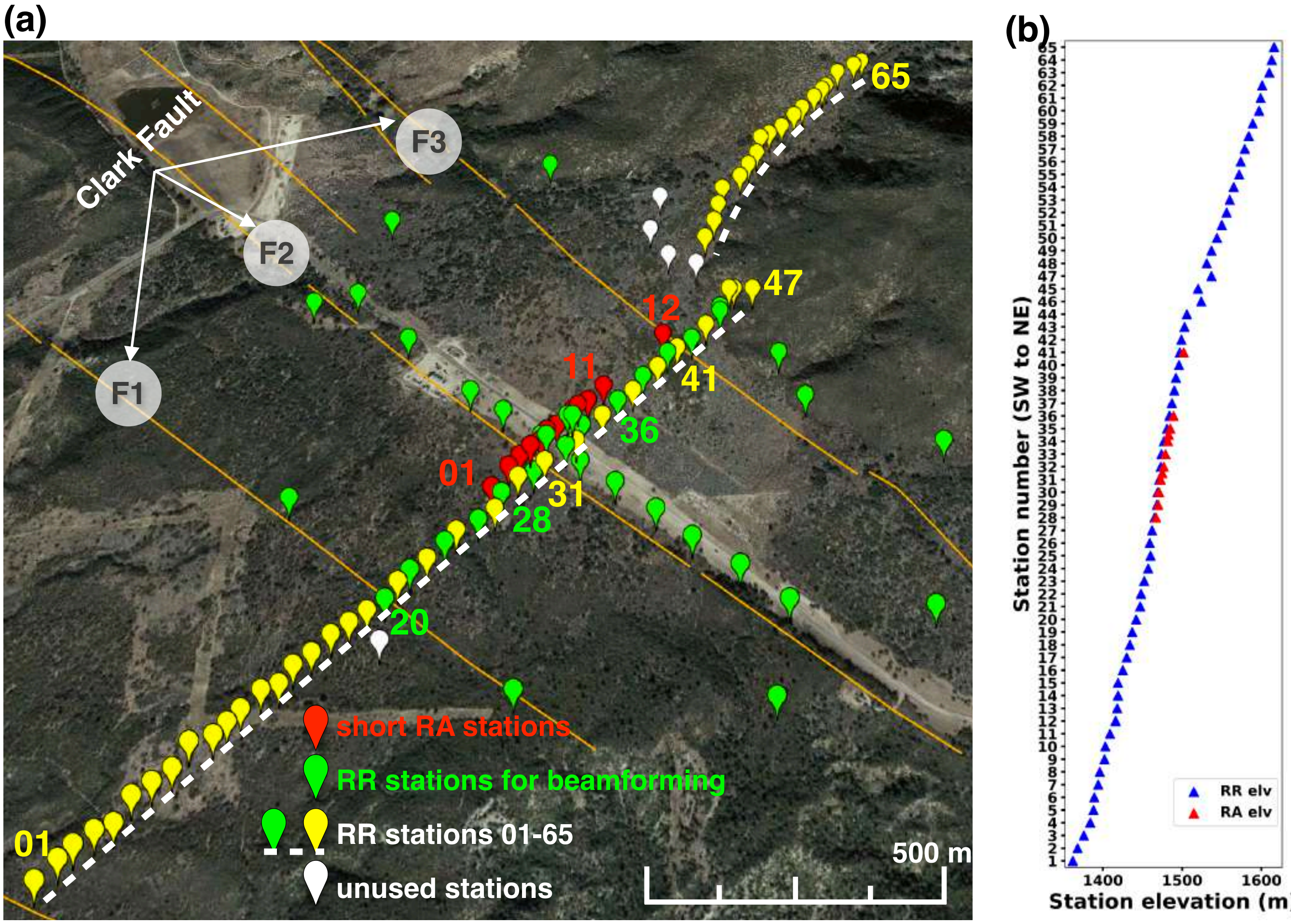

Figure 2. (a). Layout of the short RA (red balloons) and long RR (non-red balloons) arrays. Several station numbers are labeled with the same color of the station symbol. The station numbers increase from SW to NE, 01-12 for the RA and 01-65 (following the white dashed lines) for the RR arrays. Green balloons are RR stations used for beamforming. The orange lines represent the three fault surface traces of the Clark Fault that are related to previous M > 6 earthquakes, labeled as F1, F2, and F3. (b). Station elevation profiles for the RR (blue triangles) and RA (red triangles) arrays.

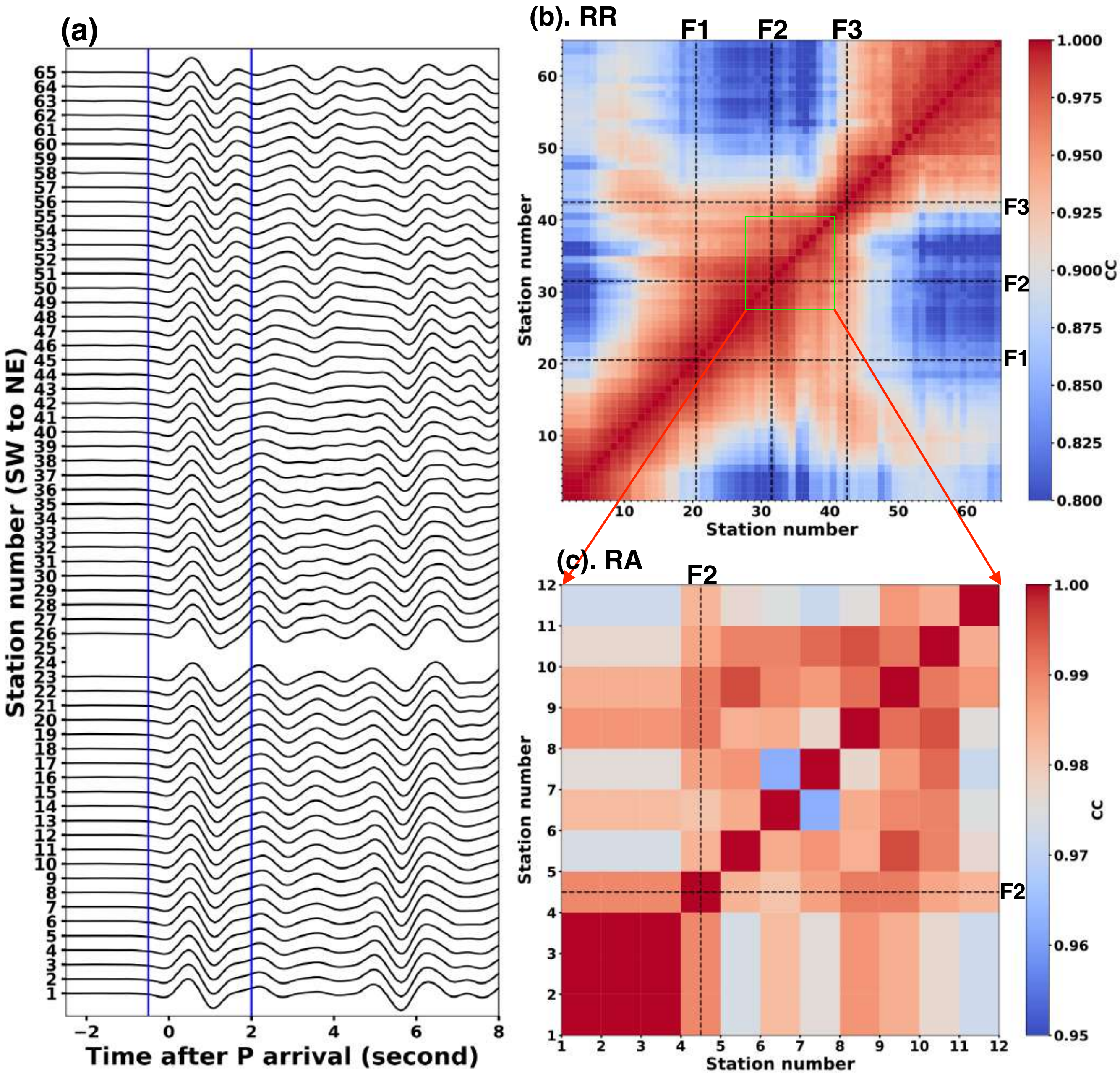

Figure 3. (a). 1 Hz lowpass filtered waveforms from event Tele1 (labeled in Fig. 1b). Zero time indicates P arrival, and blue lines represent the 2.5 second time window for cross correlation. Low SNR traces are removed. (b) and (c) are the median cross correlation coefficients of the RR (b) and RA (c) arrays from all the teleseismic events. The locations of three fault surface traces (F1, F2, F3) are plotted with black dashed lines.

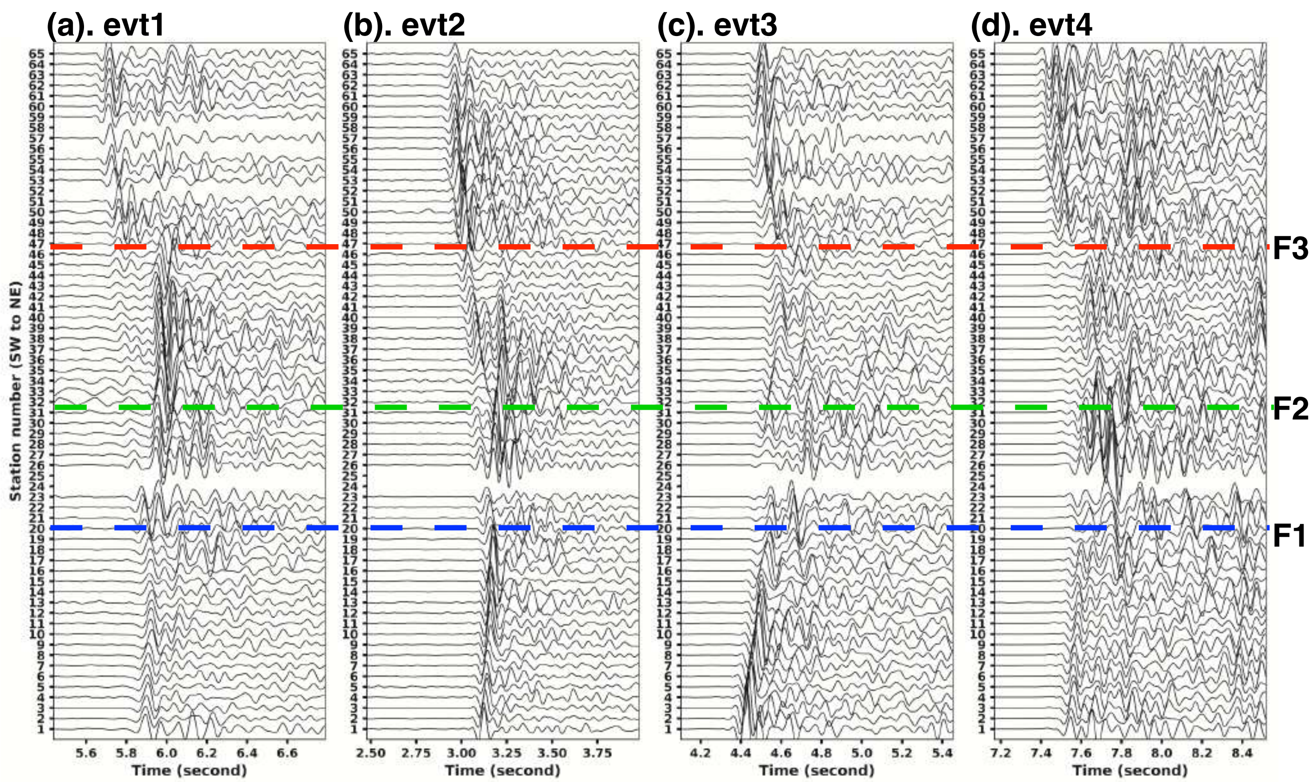

Figure 4. 1-20 Hz bandpass filtered waveforms from four local events (evt 1-4, labeled in Fig. 1a). Locations of the three fault surface traces (F1, F2, F3) are labeled.

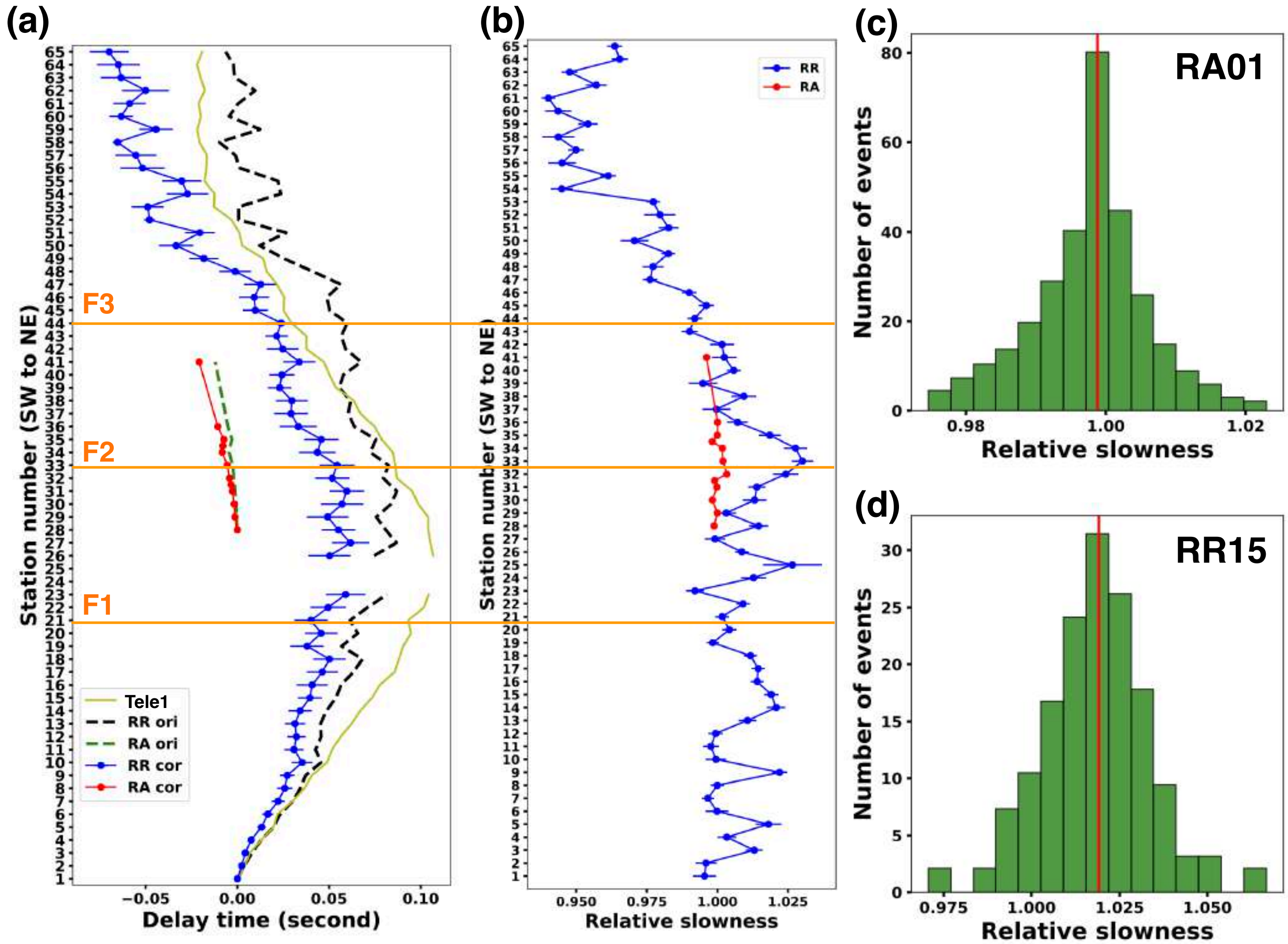

Figure 5. Delay time analysis results from teleseismic events (a) and relative slowness analysis from local events (b-d). (a). Teleseismic P wave delay time results from a single event Tele 1 (faded green line labeled as "Tele1"; event location is labeled in Fig. 1b and waveforms are shown in Fig. 3a), median delay time from all events at the RR (black dashed line) and RA (green dashed line) arrays, corrected median delay time using v_{ref}=4 km/s at the RR (blue dots) and RA (red dots) arrays with error bar being one standard error. (b). Relative slowness from local earthquakes at the RR (blue dots) and RA (red dots) arrays. Error bar is one standard error. (c) and (d) show histograms and median values (red lines) of relative slowness at stations RA01 and RR15, respectively.

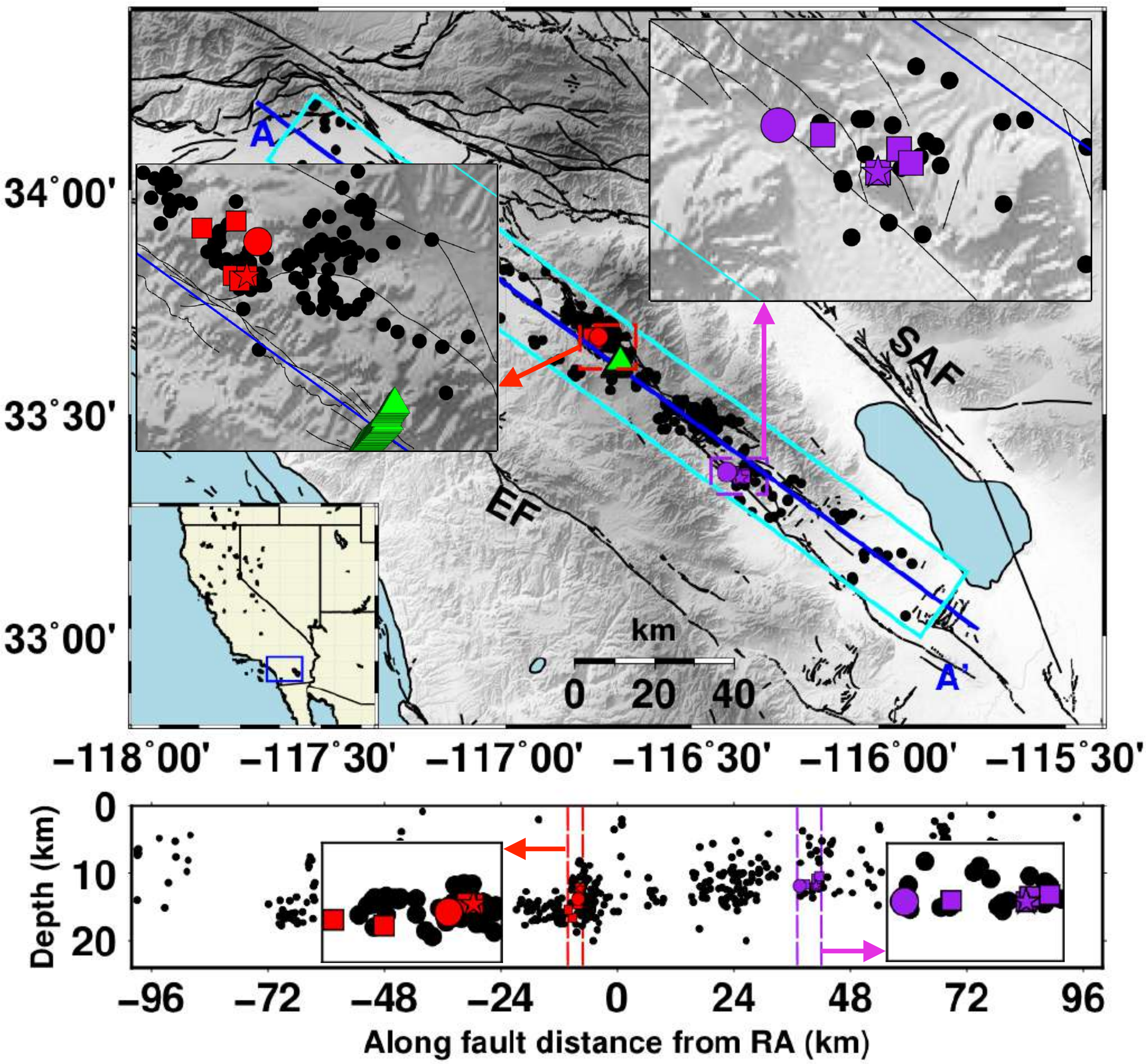

Figure 6: Events that generate local (red squares) and regional (purple squares) FZHW. The red star and circle represent the candidate and reference events for local FZHW (Fig. 7), and purple star and circle for regional FZHW (Fig. 9).

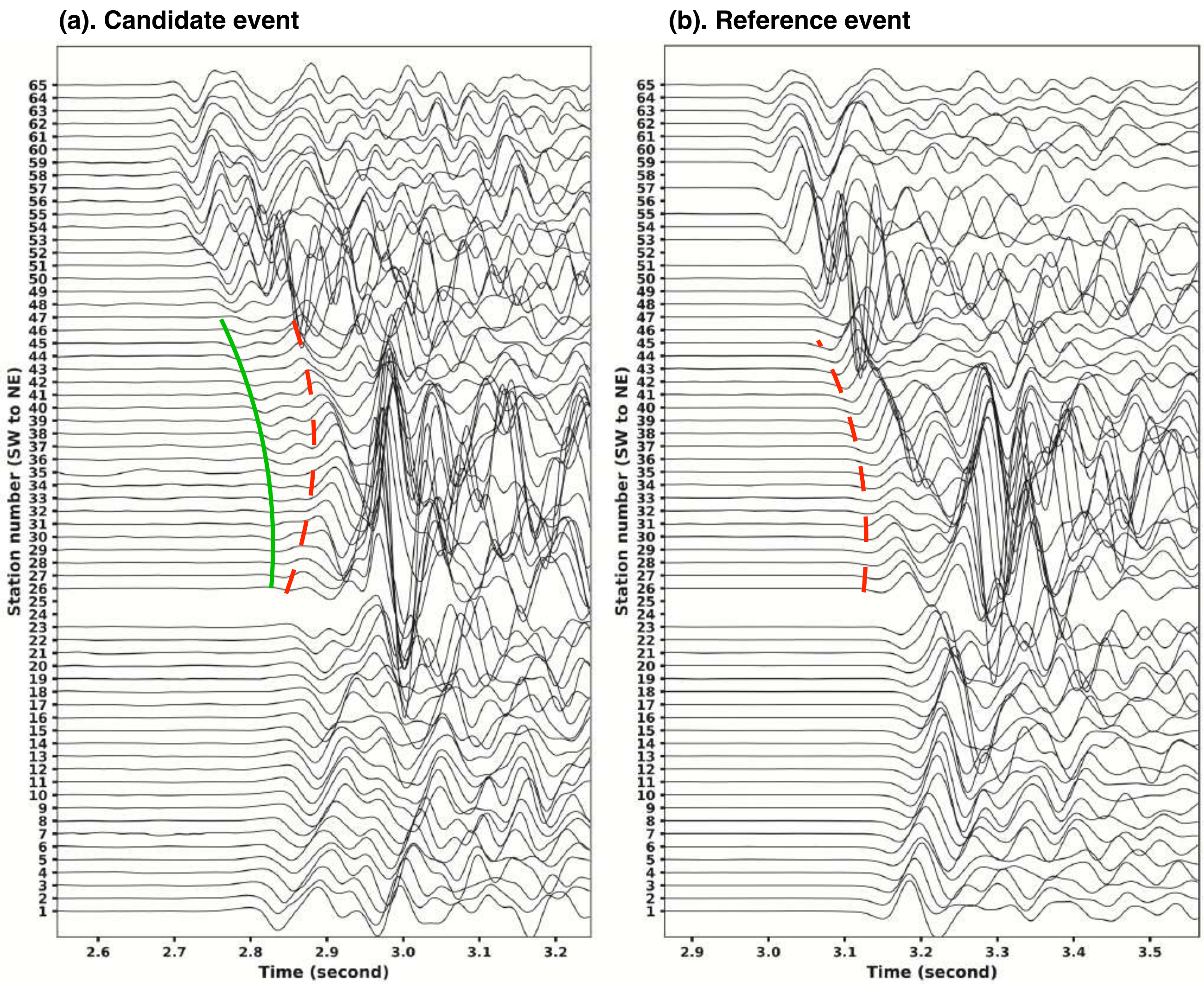

Figure 7: 1-20 Hz bandpass filtered waveforms from a candidate event (a; red star in Fig. 6) with and a reference event (b; red dot in Fig. 6) without local FZHW. Green and red dashed lines show the FZHW and impulsive P arrivals, respectively. Waveforms from each event are uniformly normalized by the array maximum, and zero time corresponds to event's origin time.

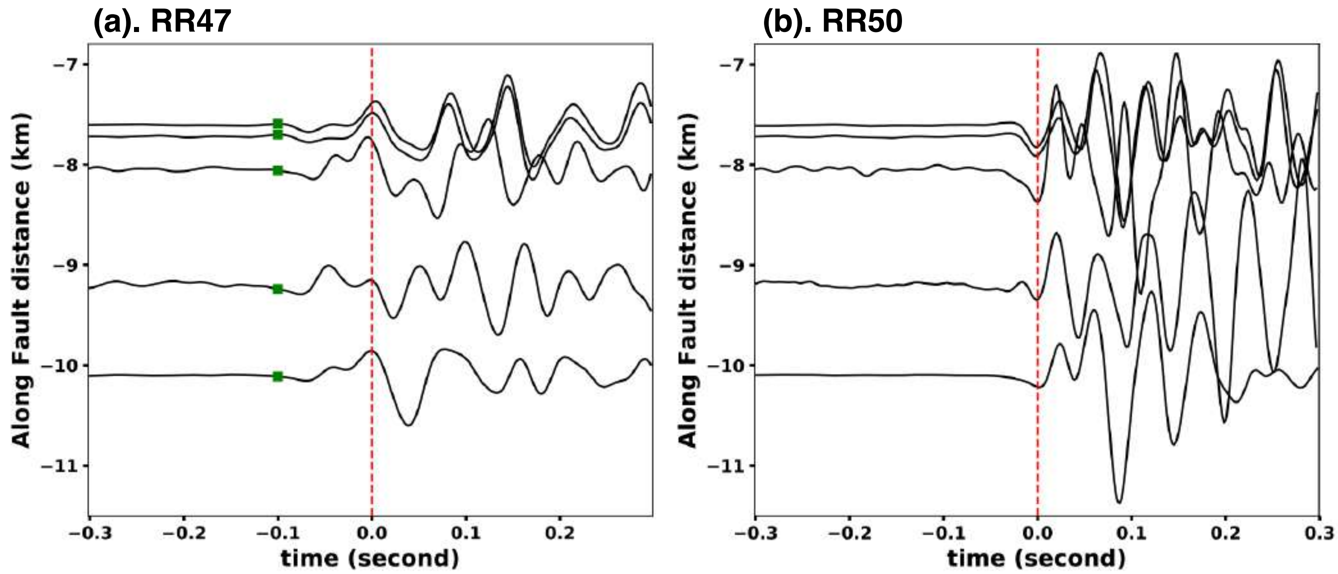

Figure 8: Waveforms at stations RR47 (a) and RR50 (b) from all events (red squares in Fig. 6) that generate local FZHW. FZHW arrivals are labeled with green squares. Waveforms are normalized by the array maximum for each event to preserve the amplitude information, and aligned according to the first impulsive waves, i.e. direct P arrivals (zero time, red dashed lines).

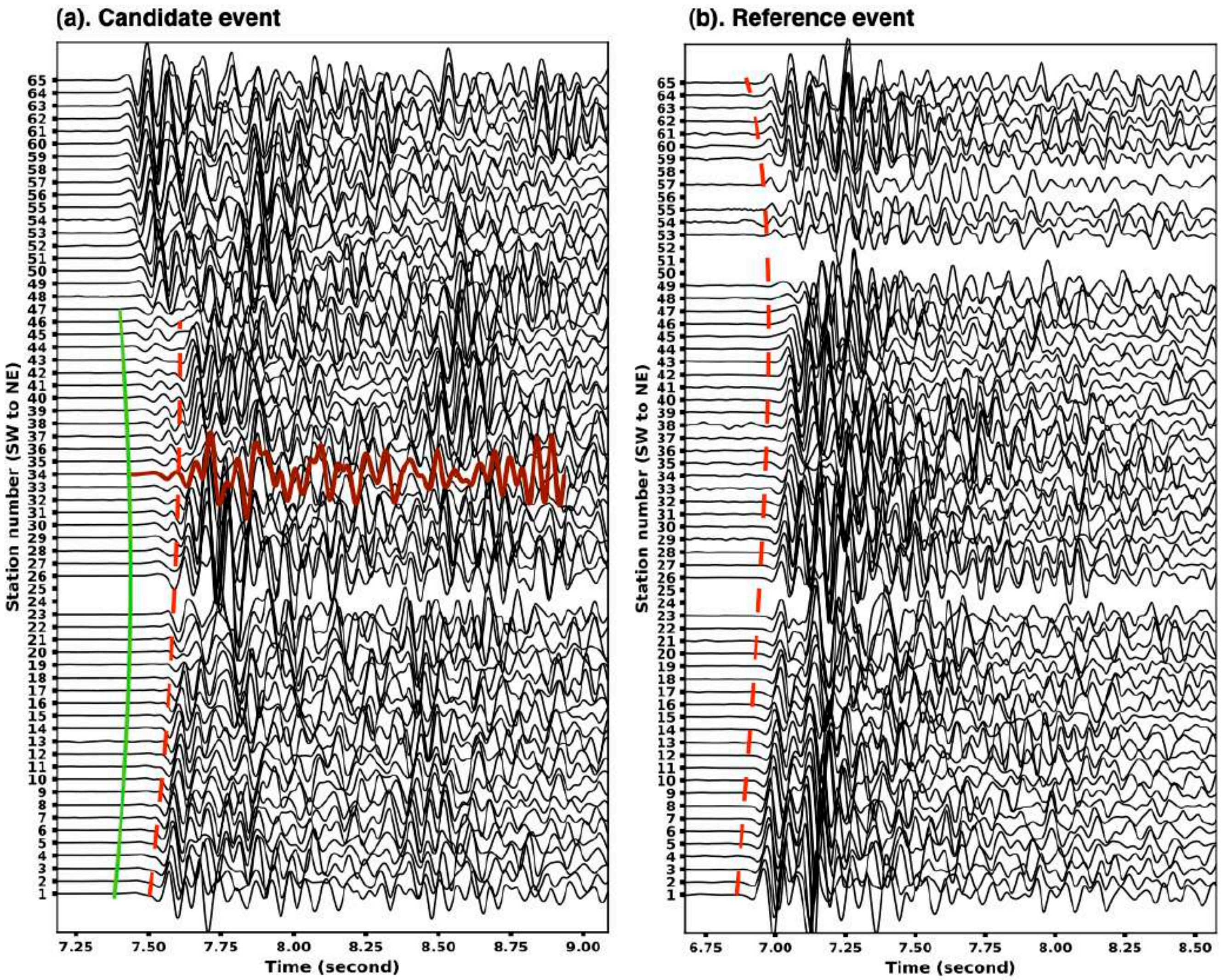

Figure 9. 1-20 Hz bandpass filtered waveforms from a candidate event (a; purple star in Fig. 6) with and a reference event (b; purple dot in Fig. 6) without regional FZHW. The layout is the same as in Fig. 7, but a longer time window is shown to highlight the original 1.5 s reference beam trace for the central station RR34 (dark red) associated with the frequency windowed beam stacks in Fig. 11(c).

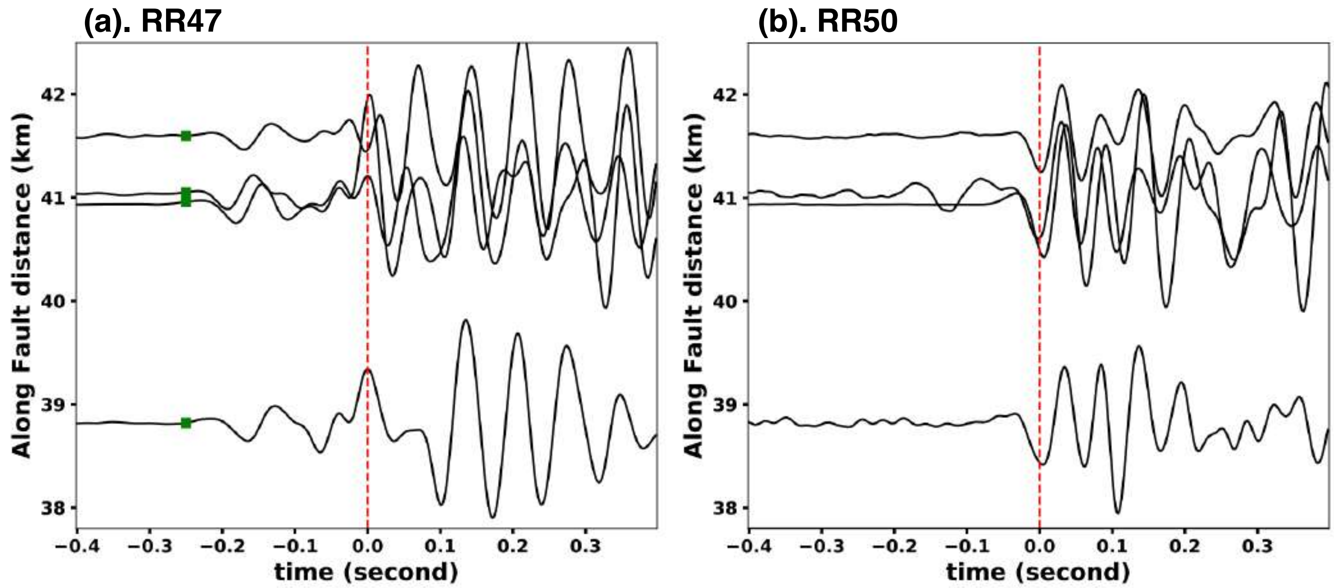

Figure 10. Waveforms at stations RR47 (a) and RR50 (b) from all events (purple squares in Fig. 6) that generate regional FZHW. The layout is the same as in Fig. 8.

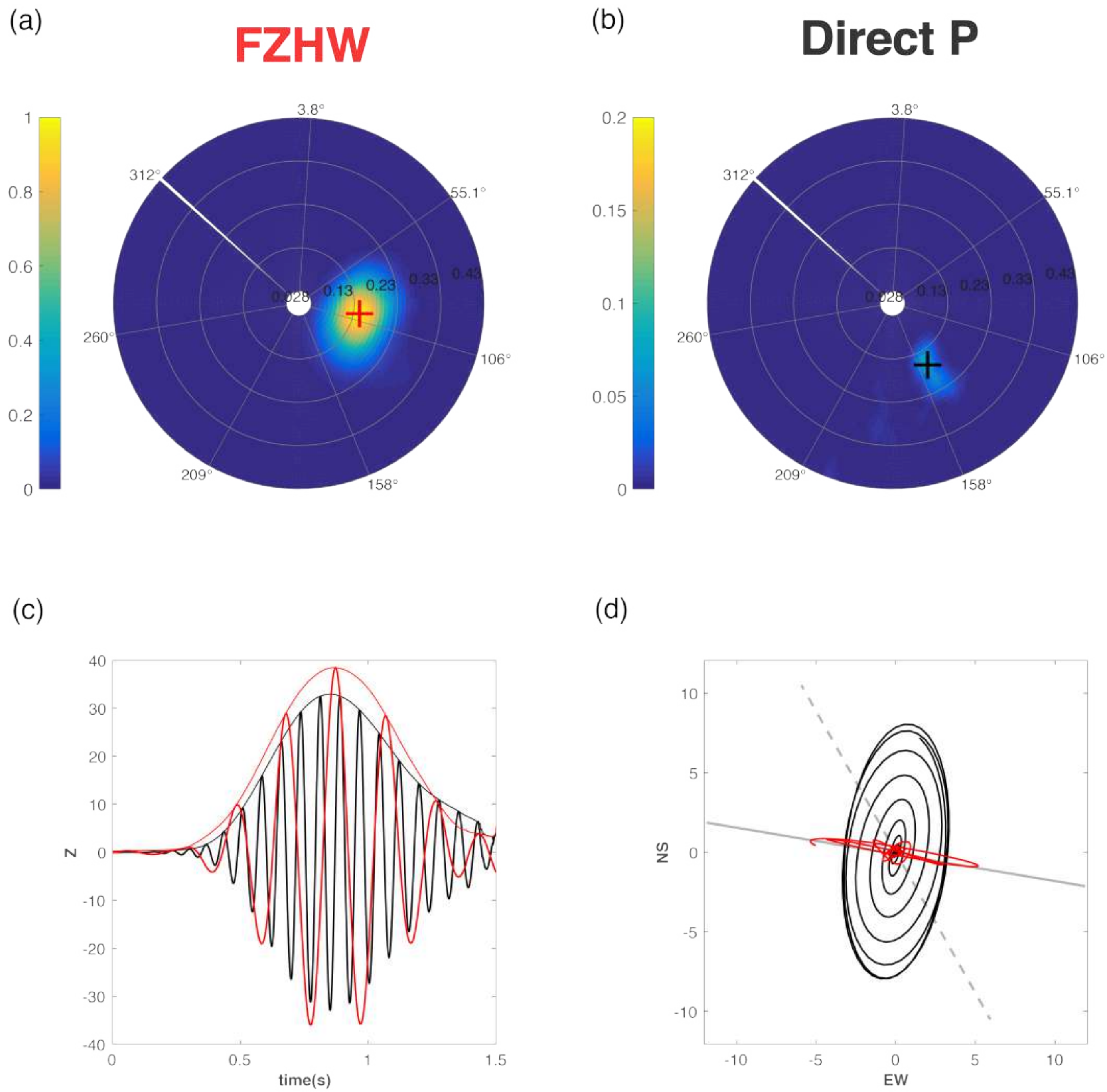

Figure 11. Separation of FZHW and direct P wavefronts using beamforming. (a). Beamforming results for the frequency band 4-6 Hz. The red cross represents a prominent coherent phase within the FZHW spectrum. Radius of this beam to 50% of peak amplitude corresponds to a slowness difference of ~0.05 s/km. (b). Beamforming results for the frequency band 12-14 Hz. The black cross represents a prominent coherent phase within the direct P wave spectrum. The beam radius here corresponds to a slowness difference of ~0.03 s/km. (c). Beam traces and energy envelopes for the beamforming results in (a) (red) and (b) (black). (d). Horizontal particle motions for the FZHW beam trace (red) and direct P beam trace (black) compared to their respective azimuths determined in (a) (gray solid line) and (b) (gray dashed line).

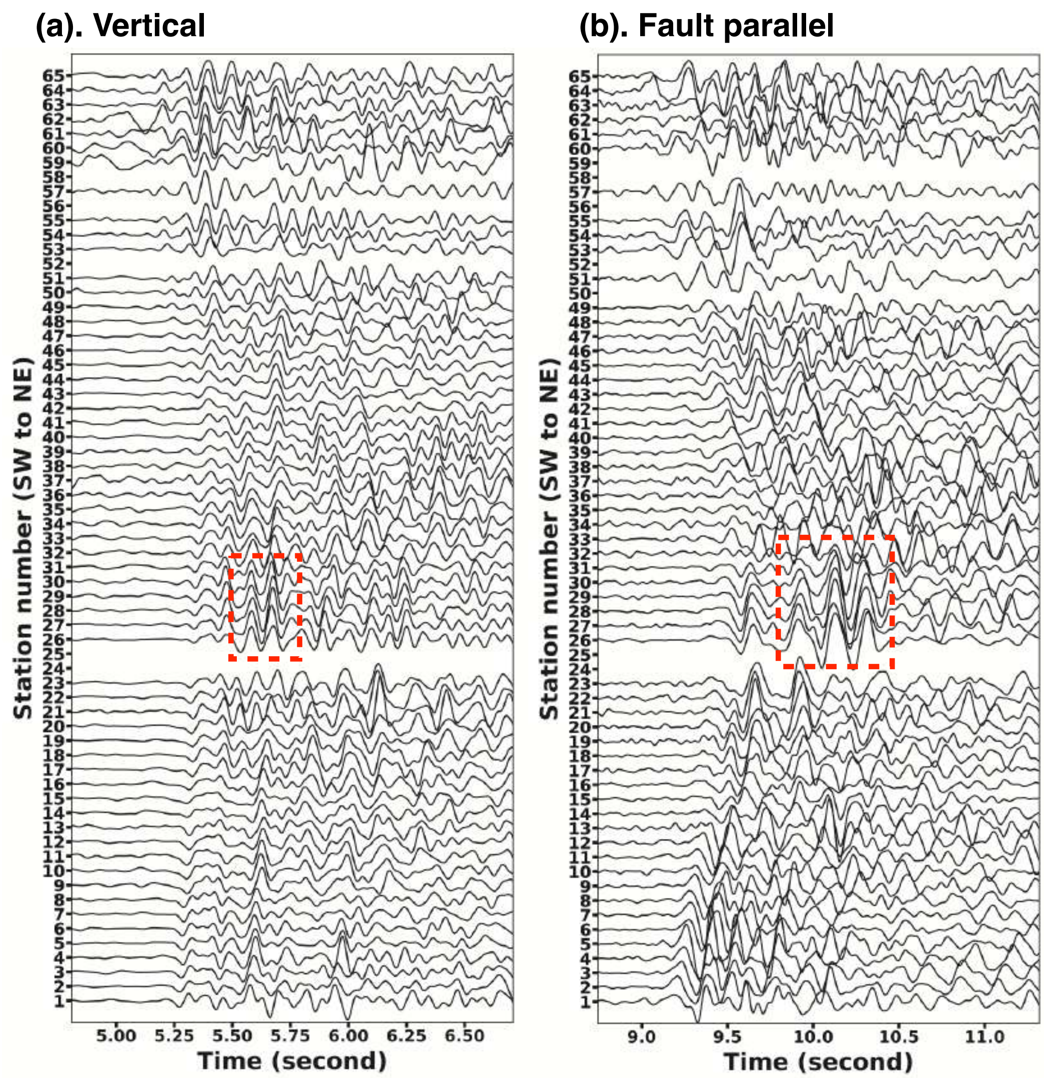

Figure 12. Vertical (a) and fault parallel (b) component waveforms from the FZTW candidate event TW1 (labeled in Fig. 1a). P- and S- type FZTW are labeled with red dashed boxes.

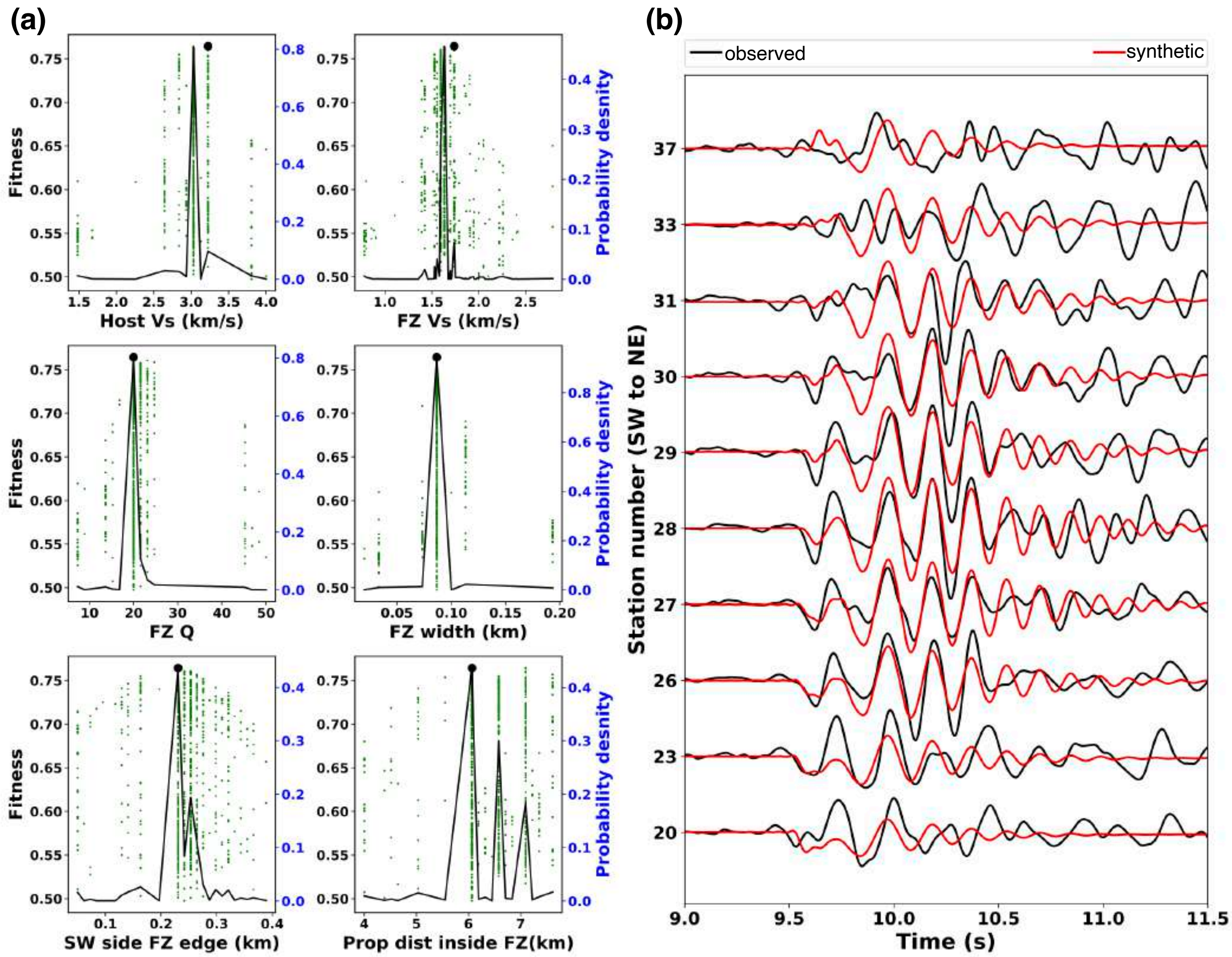

Figure 13. S-type FZTW inversion results from event TW1. (a). Parameter space plot from the last 2000 inversion models showing the fitness values (green dots), probability density functions (black curves), and best fitting model (black dots). From top to bottom (left to right) shows the shear wave velocity of host rocks, and shear wave velocity, Q value, width, SW edge and propagation distance of FZTW inside the damage zone. (b). Observed (black) and synthetic (red) waveforms from the best-fitting model (black dots in a).

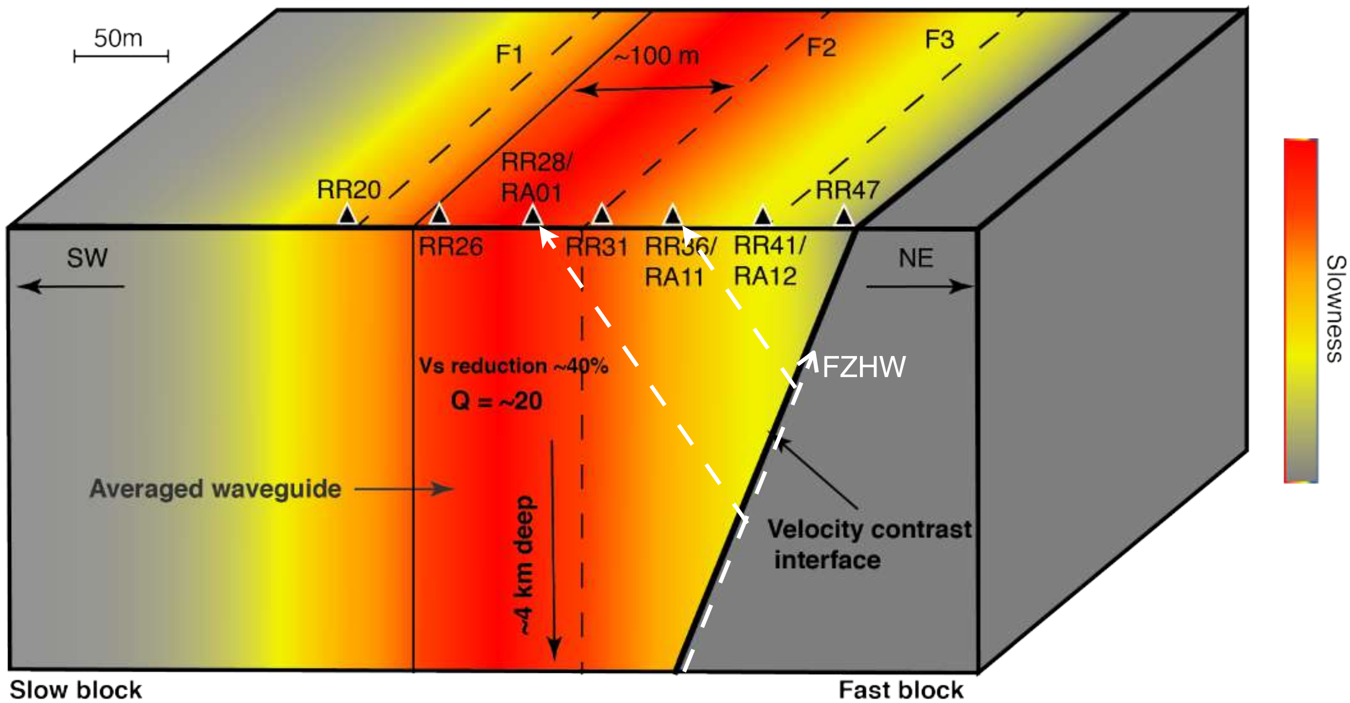

Figure 14. A schematic local velocity model at the study site.

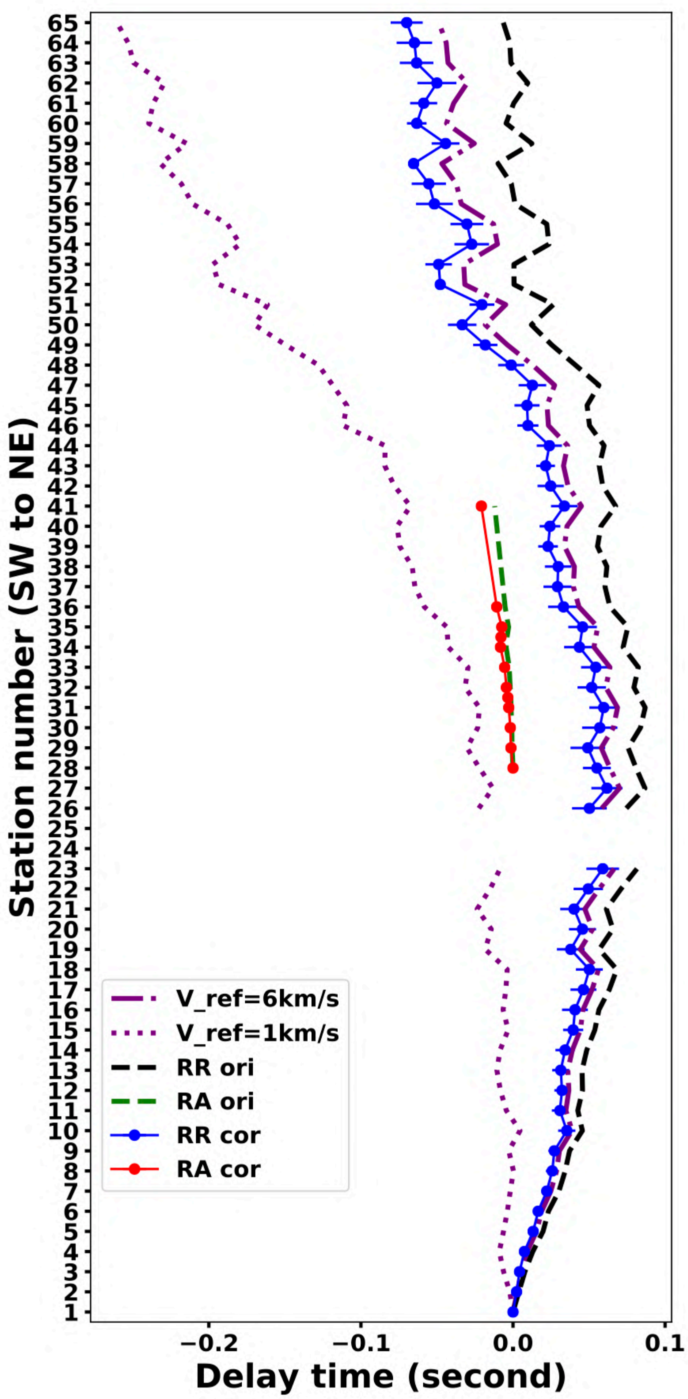

Figure S1. Teleseismic P wave delay times corrected with two extreme reference velocities: 1 km/s (purple dotted line) and 6 km/s (purple dash dotted line). Other symbols are the same as in Fig. 5(a).

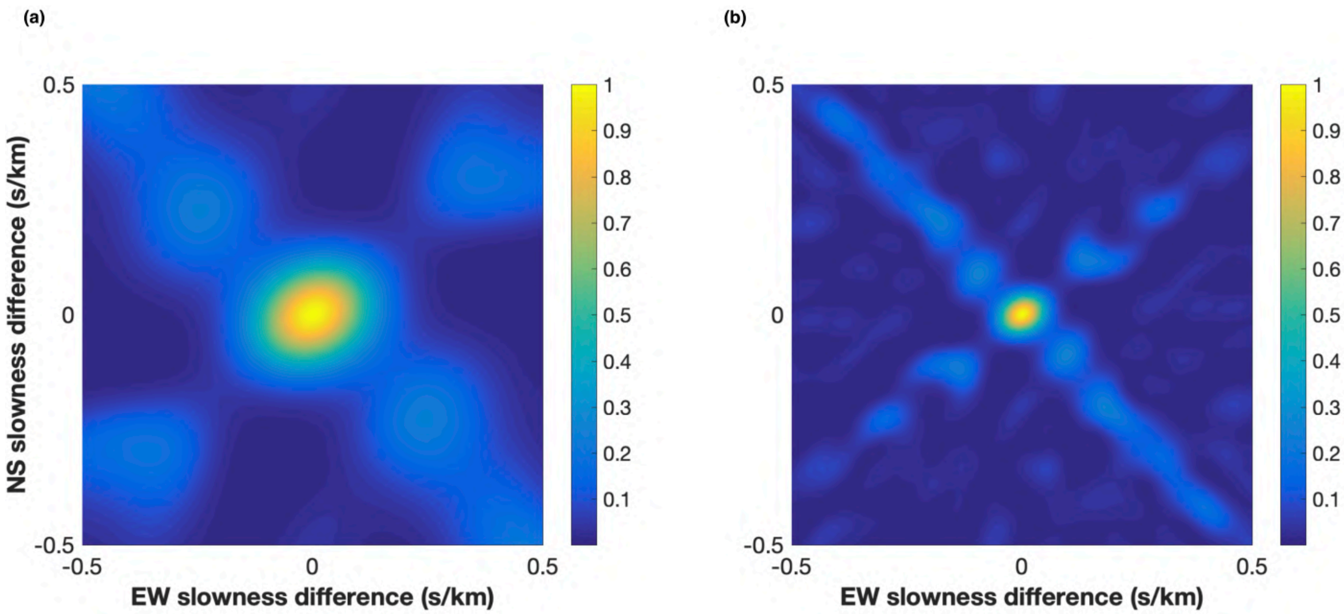

Figure S2. Array transfer functions for the array geometry employed in beamforming analysis (green balloons in Fig. 2) and frequency ranges 4-6 Hz (a) and 12-14 Hz (b). The average radii of the respective beams (measured out to 50% of the beam peak amplitude) are 0.1 s/km (a) and 0.04 s/km (b).

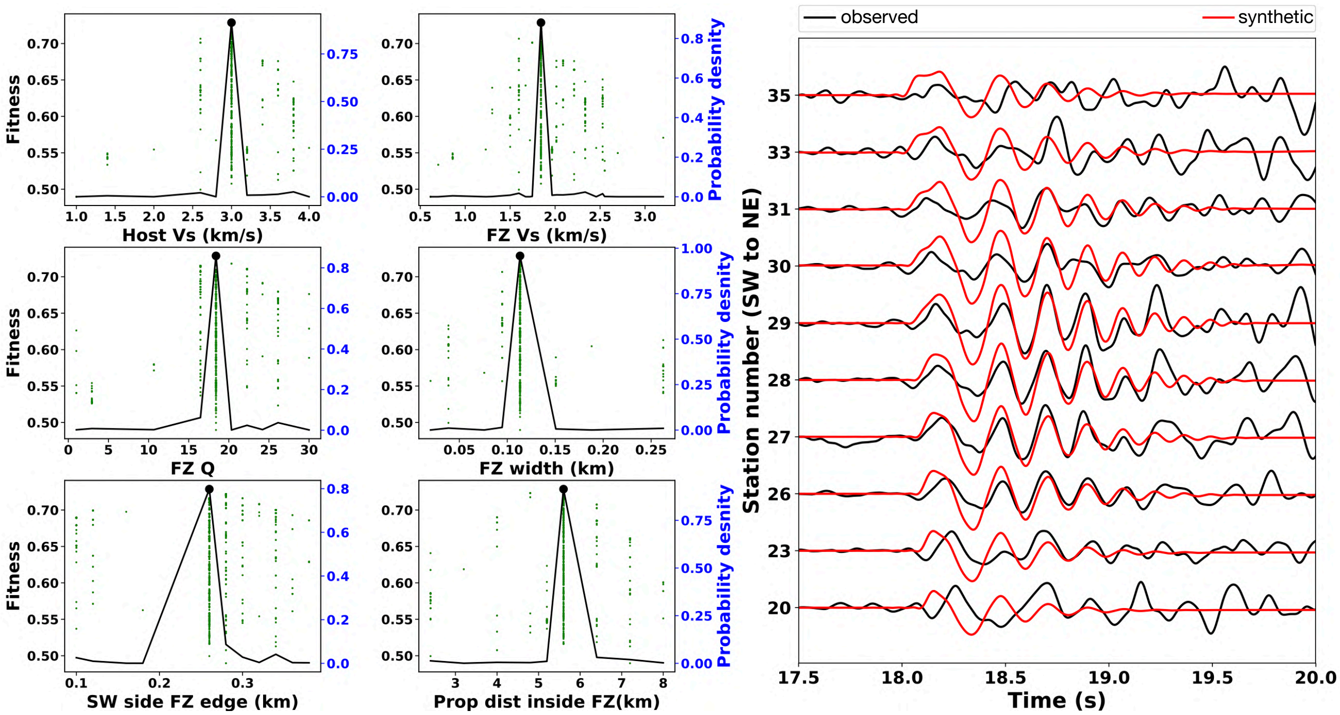

Figure S3. S-type FZTW inversion results from an example event. The layout is the same as in Fig. 13.

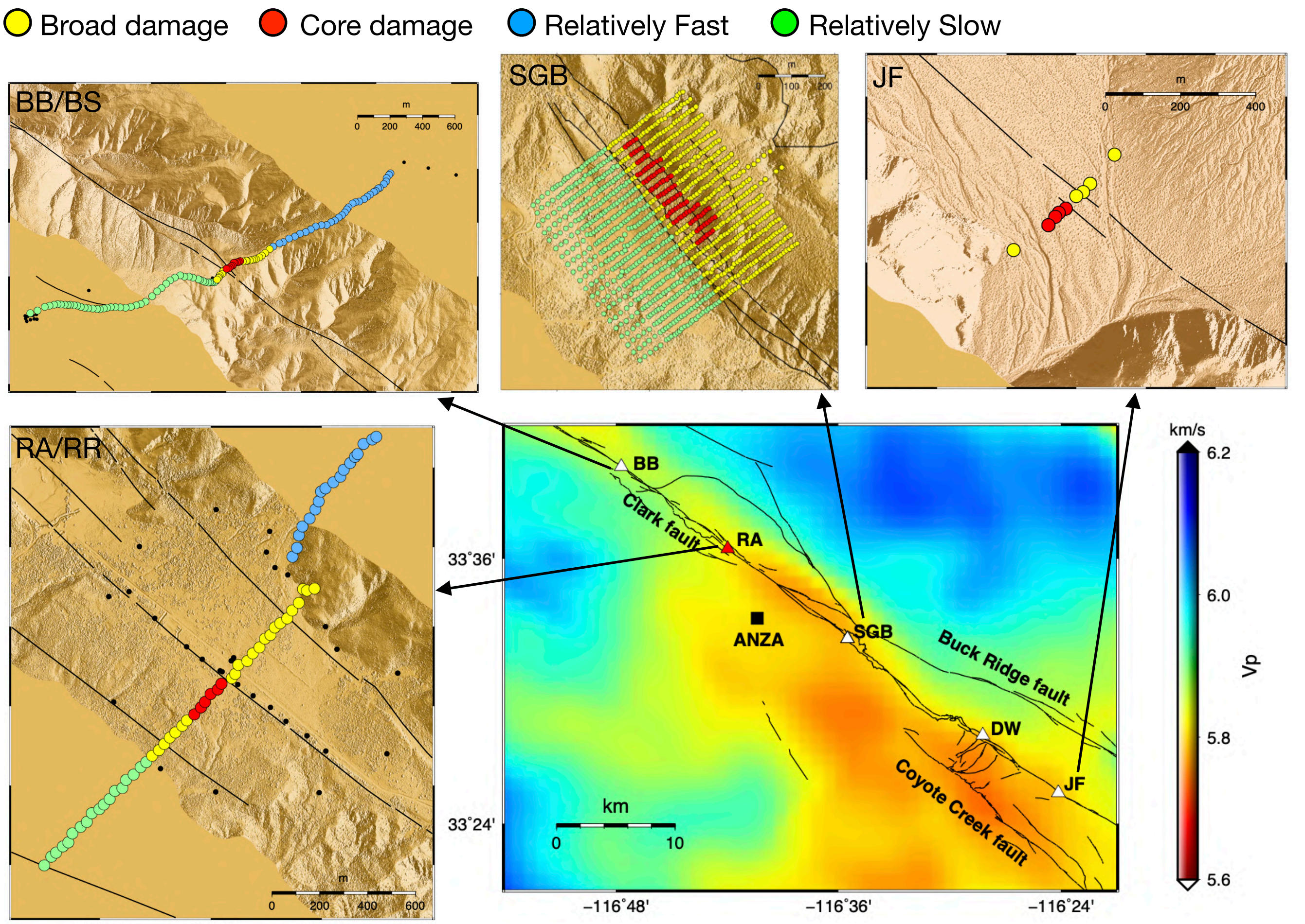

Figure S4. Regional P-wave velocity model (Allam & Ben-Zion 2012) averaged over the depth range 1-10 km, surrounded by qualitative comparisons between the regions and dimensions of internal San Jacinto fault zone structures at the different BB/BS (Share *et al*. 2017; Share *et al*. 2019b), RA/RR (this study), SGB (Ben-Zion *et al*. 2015; Qin *et al*. 2018) and JF (Qiu *et al*. 2017) sites.